

1
2 **Optimum control parameters and long-term productivity of geothermal**
3 **reservoirs using coupled thermo-hydraulic process modelling**
4

5 **Musa D. Aliyu¹ and Hua-Peng Chen^{1*}**

6 *¹Department of Engineering Science, University of Greenwich, Chatham,*

7 *Kent ME4 4TB, U. K.*

8 *Email: m.d.aliyu@greenwich.ac.uk*

9 **Corresponding author: H.Chen@greenwich.ac.uk*
10

11 **Abstract**

12 Knowing the long-term performance of geothermal energy extraction is crucial to decision-
13 makers and reservoir engineers for optimal management and sustainable utilisation. This article
14 presents a three-dimensional, numerical model of coupled thermo-hydraulic processes, in a
15 deep heterogeneous geothermal reservoir overlain and underlain by impermeable layers, with
16 discrete fracture. The finite element method is employed in modelling the reservoir, after
17 conducting a verification study to test the capability of the solver and the results obtained are
18 in agreement with the existing models. The model is then used to investigate the responses of
19 human control parameters (injection flow rate, fluid injection temperature, and lateral well
20 spacing) on reservoir productivity, using different operation scenarios. The injection flow rate
21 is found to be more efficient, concerning reservoir productivity, than the other two parameters.
22 To this end, the study concludes that, by varying some parameters in the subsurface, reservoir
23 productivity can be optimised efficiently. The numerical model developed provides in-depth
24 insight to stakeholders and reservoir engineers concerning the essential parameters to control
25 during exploration and exploitation.
26

27 **Keywords:** geothermal energy extraction, coupled thermo-hydraulic, discrete fracture, finite
28 element method, parameters analyses
29
30

31 **1. Introduction**

32 Geothermal energy is a base load energy resource that is available universally beneath us in
33 great quantity. One form of this resource is the deep geothermal system, from which energy is
34 mined by forcing circulating fluids via an injection well to create a reservoir and then extracting
35 the fluid back through a production well in a closed loop [1]–[4]. Before exploiting the energy,
36 preliminary studies on the geological formations and petrophysical properties of a selected field
37 needed to be conducted. However, field experiments are very expensive to perform [5], and the
38 long-term performance of the systems should be investigated before engagement. Numerical
39 modelling can provide essential information that will guide in determining the long-term
40 performance of geothermal systems. To simulate and evaluate the behaviour of a deep
41 geothermal system for its commercial viability, a reliable numerical method that can handle
42 the complexity of subsurface flow is needed [6]. The modelling of geothermal systems has
43 become a useful technology with applications to more than 100 fields worldwide [7]. Also,
44 computational meshes of large, complex, three-dimensional models with more than 4000
45 blocks are now used routinely [7]. The first development of a geothermal reservoir simulation
46 took place in the early 1970s [8]. However, the most accepted one in the geothermal industry
47 was the 1980 code comparison exercise organised by the US Department of Energy [9], which
48 consisted of testing several geothermal simulators on a set of six test problems. As a result, a
49 progressive improvement in the capabilities of simulation codes for geothermal reservoir
50 modelling has been acquired.

51 There have been substantial advances in numerical simulation for geothermal reservoirs
52 over the past several decades, with the steady growth of computational power and the
53 development of numerical models that have minimised several simplifying hypotheses. The
54 advances include the implementation of more accurate equations of state for the fluid system,
55 for instance, in the TOUGH2 and TOUGHREACT codes and the FALCON code [10]–[12].
56 Also, there has been tremendous progress in the ability to represent geometric complexity and
57 heterogeneity in simulation codes; examples include FEFLOW, GOCAD, and OpenGeoSys
58 [13], [14]. Computational schemes that are faster and more accurate have also been elaborated
59 in reservoir simulation. Other numerical simulation codes are still under development,
60 especially those by the current reservoir modelling working group, inaugurated with the help
61 of the International Partnership for Geothermal Technology (IPGT). The IPGT is an
62 international organisation with five member countries (Australia, Iceland, New Zealand,
63 Switzerland, and the United States) aiming to improve understanding of geothermal potentials
64 and usage in the globe [15]. The organisation proposed to develop a standard geothermal

65 simulation code that will couple the various interactions arising during exploitation by the year
66 2020. The Geothermal Technology Office (GTO) under the Energy Department of the United
67 States has initiated a code comparison study program that will improve the state of the art of
68 geothermal simulation codes [16]. The program focused on examining existing codes,
69 identifying dissimilarities, and illustrating the modelling capabilities of a global compilation
70 of several numerical simulators for assessing geothermal technologies. Six benchmark
71 problems were proposed, and the program commenced in 2014. According to White and
72 Phillips [17], 12 groups participated in the challenge, and each group had a unique numerical
73 simulator and analytical approaches providing a detailed mechanistic approach, modelling
74 process, and solution scheme. Ghassemi et al. [18] reported on some of the outcomes of the
75 program, stating that none of the 12 members was able to participate in all six problems due
76 specifically to code limitations.

77 Therefore, geothermal modelling tools exist for several decades, but they were unable
78 to cope with modern demands, both in resolving scientific and resource specific questions and
79 in computational practicability [19]. Although concepts can be rigorously tested for
80 consistency with data as soon as these become available, it is never early to establish a
81 computational model [18]. An appropriate numerical modelling tool is vital in planning the
82 energy extraction operations. The essential key instruments in planning the operations include
83 parametric studies. Shook [21] conducted an extensive study on some naturally occurring
84 parameters and their effect on energy recovery using the TETRAD code by employing the
85 geysers' geothermal data. The parameters include capillary pressure and relative permeability
86 relationship, initial liquid saturations, fracture spacing, and geologic structure. Nalla et al. [22]
87 studied the effect of formation properties and operational variables of wellbore heat exchangers
88 (WBHX) for enhanced geothermal systems (EGS) using the TETRAD simulation code.
89 Vacchiarrelli et al. [23] carried out a parametric study on the effects of fracture aperture and
90 fracture rotation angle on reservoir productivity by applying the GEOCRACK simulation code.
91 Recently, Chen and Jiang [24] reported the heat extraction performance of EGS using different
92 wellbore layout configurations. The layout investigated include doublet, triplet-straight line,
93 triplet-triangle, and quintuplet. Jain et al. [25] examined the effect of various wellbore
94 arrangements under different injection rates by employing the SHEEMAT simulation code.
95 The injected rates employed were 50 l/s, 100 l/s and 150 l/s, and the wellbore configurations
96 studied include doublet, triplet, and reversed-triplet. Poulsen et al. [26] analysed the effect of
97 thermal conductivity of confining beds, production rate, injection temperature, and reservoir
98 thickness on the productivity of low enthalpy geothermal reservoirs. Aliyu et al. [27] studied

99 the effect of extraction well placement on geothermal productivity using the dual porosity
100 approach.

101 Especially, not much attention has been paid to the parametric studies on human-
102 controlled parameters in geothermal energy extraction. Bedre and Anderson [28] first
103 introduced the idea by analysing naturally occurring parameters and human-controlled
104 parameters of low-enthalpy geothermal systems in the United States using the 'One Factor At
105 a Time' (OFAT) method. Saeid et al. [29] developed a prototype model capable of estimating
106 the lifetime of low-enthalpy systems, based on the OFAT method proposed in [28]. In [28] the
107 reservoir is represented as a three-dimensional (3-D) model with the assumption of a simplistic
108 porous media approach for the fracture systems using the TOUGH2 five-spot model, whereas
109 in [29], the contributions of fracture systems is ignored in their representation but an explicit
110 3D model of the reservoir is depicted with underlying and overburdened strata. It can be
111 summarised from the above literature that the previous research focuses specifically on low-
112 enthalpy geothermal systems, naturally occurring parameters, and stochastic modelling tools
113 in the reservoir representations. Thus, not much has been reported on human-controlled
114 parameters in geothermal energy extraction, more specifically on enhanced geothermal
115 systems with open boundaries.

116 In this study, a 3-D numerical model of a deep and heterogeneous geothermal reservoir
117 is developed with a discrete fracture using the Soultz EGS scheme. The system proposed here
118 considers the influence of the surrounding media, the reservoir, and the fractures concurrently
119 in the estimation of the effect of human control parameters on geothermal energy extraction.
120 In this model, the fluid is circulated through an inclined vertical well connected to the matrix
121 (i.e., not a fracture) in a fully saturated porous medium, unlike the previously reported models
122 in which the injection and the production wells communicate via a single planar fracture or
123 multiple. Although, a fracture is also included in this model that intersects the matrix at an
124 angle but without connecting the wellbores to communicate. The reason for these assumptions
125 in the current model is that sometimes the wellbores do not connect through fractures, as in the
126 case of Soultz triplet geothermal reservoir where a low connection between GPK3 (injection
127 well) and GPK4 (the second production well) is experienced due to calcite deposition [30].
128 Moreover, the geothermal reservoir is modelled as an open system that allows for additional
129 sources or losses from the surrounding boundaries. As a result, water losses in the reservoir are
130 accounted for in the model. The significance of this assumption can be supported by a real-life
131 case of an existing geothermal reservoir. For instance, the five-month circulation test regarding
132 hydraulics, conducted in the Soultz geothermal reservoir during 2005, showed that only 30%

133 of fluid mass injected is recovered at the production wells, displaying the open nature of the
134 reservoir [31]. The test result opposed the hot dry rock (HDR) concept that considered the
135 reservoir to be a closed system with no naturally existing fluid present before its injection [32].

136 The contribution of the present work includes these three aspects. First, this study has
137 proposed a mixed transport of fluid and heat in the reservoir from both the matrix block and
138 the fracture, respectively. Second, the 3-D model takes into account the effect of fluid losses
139 or gains concerning the nature of open systems in subsurface media, whose long-term influence
140 on the extraction wellbore temperature cannot be underestimated for a 30-year extraction
141 period. Third, in this investigation, each of the human-controlled parameters (injection flow
142 rate, injection temperature, and lateral well spacing) are examined under different operational
143 scenarios with other parameters. For example, injection flow rate in this study ranges from 20
144 l/s to 70 l/s. Therefore, when examining the effect of the injection flow rate on production,
145 different cases of injection temperature and well spacing are considered, because their impact
146 can also affect reservoir productivity.

147 The model addresses the limitations of previous research, which ignored the influence
148 of fractures, reservoir representation, open boundaries influence, and the inclusion of different
149 operational schemes. The study estimates the consequence of individual parameters on others
150 and their corresponding influences on the productivity of a geothermal reservoir. Solving the
151 structure of this heterogeneous system, which is nonlinear in parameters and has a coupled
152 interaction in nature, requires the use of a powerful numerical solver. The finite element
153 method (FEM) is adopted here because of its robustness in dealing with such problems. The
154 FEM package employed in the study is COMSOL with a link to MATLAB that serves as a
155 framework for implementing the numerical model and making the required coupling between
156 the physics [33]. At the end, numerical studies are carried out to verify the developed model,
157 and sensitivity analyses are performed to investigate the influence of the parameters on
158 reservoir productivity.

159

160 **2. Modelling thermo-hydraulic coupled problems**

161 The first step in the analysis of coupled fluid flow and heat transport problems consists of
162 defining the geometry, material properties, initial and boundary conditions [34]. The geometry
163 can be created or imported from a CAD program once it is developed by including the material
164 properties and initial and boundary conditions. The next step is defining the mathematical
165 model and coupled processes to be solved. The final two stages are independent of the type of

166 numerical technique employed in solving the mathematical model except that the chosen
167 solution procedures should be capable of solving the model accurately.

168 Modelling geothermal energy exploration and exploitation requires coupling the
169 complex interaction occurring among different phenomena in the subsurface. These
170 phenomena include fluid flow, heat transport, chemical transport and mechanical deformation.
171 However, this study is limited to the coupled processes of heat transport and fluid flow in a
172 fully saturated and fractured porous media. Figure 1 presents the two-way coupled approach
173 used in this study, the illustration showed the hydraulic process is affected by temperature
174 gradient directly through the change in density and viscosity of the fluid, and the thermal
175 process, on the other hand, is influenced by the convective heat transfer through Darcy's
176 velocity term. For further details on coupled processes in the field of geosciences see [35].

177

178 The macroscopic governing equations describing the behaviour of the fully coupled TH model
179 demonstrated in the previous section compels the application of conservation laws of energy
180 and mass. In this study, the derived equations are based on a dual porosity-permeability model
181 (the model that accounts for rock matrix and fracture properties as a separate continuum).
182 Therefore, this section will derive the partial differential equations for both the fluid flow and
183 heat transport using the dual porosity-permeability approach are given here.

184 The law of conservation of mass governs the fluid flow expression in porous media,
185 and the law states that the mass inflow subtracted by the mass outflow is equal to the total mass
186 accumulated by a system. Thus, the conservation of mass fluid in porous matrix system is

$$187 \quad \frac{\partial}{\partial t}(\rho_L \phi) + \nabla \cdot (\rho_L v) = 0 \quad (1)$$

188 where $\nabla \cdot$ is the divergence operator, $\rho_L v$ is the fluid mass flux and $\rho_L \phi$ is the mass per unit
189 volume within the matrix. The term ρ_L is the fluid density, ϕ is the matrix porosity and v is
190 the Darcy's flux or velocity, which is defined as

$$191 \quad v = \frac{\kappa}{\mu} (-\nabla P + \rho_L g \nabla z) \quad (2)$$

192 where κ is the intrinsic permeability of the matrix, μ is the dynamic viscosity, P is the fluid
193 pressure, g is the acceleration due to gravity, and z is the elevation. Substituting equations (2)
194 into (1) and rearranging gives

195
$$\frac{\partial}{\partial t}(\phi\rho_L)+\nabla\cdot\rho_L\left[\frac{\kappa}{\mu}(-\nabla P+\rho_L g\nabla z)\right]=0 \quad (3)$$

196 Expanding the first term in the equation (3) by expressing the porosity and density as functions
 197 of the fluid pressure, and applying the product rule and chain rule of differentiation yields

198
$$\frac{\partial}{\partial t}(\phi\rho_L)=\phi\frac{\partial\rho_L}{\partial P}\frac{\partial P}{\partial t}+\rho_L\frac{\partial\phi}{\partial P}\frac{\partial P}{\partial t} \quad (4)$$

199 Also, the equation of state (EOS) [36] defines the fluid and matrix compressibilities as

200
$$C_f=\frac{1}{\rho_L}\frac{\partial\rho_L}{\partial P}, \text{ and } C_m=\frac{1}{\phi}\frac{\partial\phi}{\partial P} \quad (5)$$

201 where C_f and C_m are the fluid and matrix compressibility, respectively. Rearranging equations
 202 (5) and inserting the terms into equation (4) yields

203
$$\frac{\partial}{\partial t}(\phi\rho_L)=\phi\rho_L(C_f+C_m)\frac{\partial P}{\partial t} \quad (6)$$

204 where $\phi(C_f+C_m)$ is defined as linearised storage S , and equation (6) becomes

205
$$\frac{\partial}{\partial t}(\phi\rho_L)=\rho_L S\frac{\partial P}{\partial t} \quad (7)$$

206 The generalised equation applied for solving problems in porous matrix is obtained by
 207 substituting equation (7) into (3)

208
$$\rho_L S\frac{\partial P}{\partial t}+\nabla\cdot\rho_L\left[\frac{\kappa}{\mu}(-\nabla P+\rho_L g\nabla z)\right]=0 \quad (8)$$

209

210 For the porous matrix with fracture, the conservation of fluid mass within the fracture system
 211 is

212
$$\frac{\partial}{\partial t}(\rho_L\phi_f)+\nabla\cdot(\rho_L v_f)+Q_f+Q_m=0 \quad (9)$$

213 The subscript's f and m refer to fracture and matrix, respectively. The term $\rho_L\phi_f$ is mass per
 214 unit volume within the fracture, $\rho_L v_f$ is defined as the fluid mass flux within the fracture and
 215 ϕ_f is the fracture porosity. The term Q_f denotes the flow from the matrix to the fracture which
 216 sometimes referred as the matrix-fracture transfer term. This term describes the flow in the

217 fracture system contains a source term that represents the transport of fluid from the matrix to
 218 the fracture that is assumed to be distributed over the entire domain. Two different approaches
 219 can be used to determine the matrix-fracture transfer term Q_f , as described in [37-39].
 220 However, in this study, the latter model [40] is chosen and is given as

$$221 \quad Q_f = - \sum \chi_i(x) \frac{1}{|\Omega_i|} \int_{\Omega_i} \frac{\partial(\phi \rho_L)}{\partial t} dx, \text{ and } \chi_i(x) = \begin{cases} 1 & \text{if } x \in \Omega_i \\ 0 & \text{otherwise} \end{cases} \quad (10)$$

222 where $|\Omega_i|$ represents the volume of the i th matrix block (i.e. Ω_i) and $\chi_i(x)$ is its characteristic
 223 function. On the other hand, the term Q_m is the external sources or sinks of fluid that may be
 224 comprised of an injection or production source and sometimes others sources/sinks from the
 225 surrounding boundaries. In this case, the expression of Q_m is adopted from [41], by assuming
 226 that the sum of the normal components of fluid flow from the matrix block through the
 227 boundary cell, given here as

$$228 \quad Q_m = - \int_{\text{cellboundary}} \nabla \cdot \frac{\kappa \rho_L}{\mu} \nabla P \cdot \bar{n} dx \quad (11)$$

229 The Darcy's flux or velocity of the fluid in an equivalent fracture system v_f , defined as

$$230 \quad v_f = \frac{\kappa_f}{\mu} (-\nabla P_f + \rho_L g \nabla z) \quad (12)$$

231 in which the fracture permeability κ_f is assumed to obey laminar flow by applying the
 232 concept of parallel plate and considering it as a uniform plate, expressed as

$$233 \quad \kappa_f = \frac{b^2}{12} \quad (13)$$

234 where b is the fracture aperture.

235 Substituting equation (13) into (12), and inserting output back into equation (9), and
 236 also replacing the first term in bracket of equation (9) by applying similar expression obtained
 237 in (7) gives the generalised expression (14) for solving fracture problems in porous media,
 238 namely

$$239 \quad \rho_L S_f \frac{\partial P_f}{\partial t} + \nabla \cdot \rho_L \left[\frac{b^2}{12\mu} (-\nabla P_f + \rho_L g \nabla z) \right] + Q_f + Q_m = 0 \quad (14)$$

240 However, it is critical to note that solving equations (8) and (14) requires boundary conditions,
 241 which are $\rho_L v \cdot n$, and $\rho_L v_f \cdot n$ for the matrix and fracture, respectively. Explicit details are
 242 provided in section 3 under the finite element formulations.

243

244 In this paper, local thermal equilibrium heat transport equations between the solid and fluid
 245 phases is considered, in which the solid temperature (T_s) is equal to the fluid temperature (T_f
 246) (i.e., $T_s = T_f = T$). Here, it is assumed that heat conduction in the solid and fluid phases occur
 247 side-by-side so that there is no net heat transport from one phase to the other. Therefore, the
 248 classical Newton's law of cooling is not applicable here, because it is very hard to estimate all
 249 the parameters included in the formula. However, it is only possible to apply the formula under
 250 laboratory conditions. The governing equation defining heat transport in porous media is the
 251 conservation of energy law expressed as

$$252 \quad \frac{\partial}{\partial t} A_E + \nabla \cdot q_E = 0 \quad (15)$$

253 where A_E is the energy per unit volume is given

$$254 \quad A_E = \phi_s \rho_s c_{\rho,s} T + (1 - \phi_s) \rho_L c_{\rho,L} T = \rho c_\rho T \quad (16)$$

255 in which ϕ_s and ϕ_L are the solid and liquid volume fraction (porosity), respectively; $c_{\rho,s}$ and
 256 $c_{\rho,L}$ are the specific heat capacity for the solid and liquid, respectively; ρ_s is the density of the
 257 solid and T is the temperature. Also, q_E is the energy flux given by

$$258 \quad q_E = \rho_L v c_{\rho,L} T + q \quad (17)$$

259 The coupled contribution of convective heat transfer is giving in the first term of the right-hand
 260 side of equation (16) while $q = -\lambda \nabla T$ is the input of conductive heat transfer referred as the
 261 Fourier's law, where λ is the effective thermal conductivity of both the solid and liquid phases
 262 expressed as $\lambda = \phi_s \lambda_s + (1 - \phi_s) \lambda_L$, in which λ_s is the solid thermal conductivity and λ_L is
 263 liquid thermal conductivity. Substituting equations (16) and (17) with their derivatives into
 264 equation (15) yields the general expression for solving heat transport in the porous matrix as,
 265 i.e.

$$266 \quad \rho c_\rho \frac{\partial T}{\partial t} + \nabla \cdot (\rho_L v c_{\rho,L} T - \lambda \nabla T) = 0 \quad (18)$$

267 Similarly, the conservation of fracture energy within a matrix block is given by

268
$$\frac{\partial}{\partial t} A_{f,E} + \nabla \cdot q_{f,E} + Q_{f,E} + Q_{m,E} = 0 \quad (19)$$

269
$$\rho c_{\rho} \frac{\partial T}{\partial t} + \nabla \cdot (\rho_L v_f c_{\rho,L} T - \lambda_f \nabla T) + Q_{f,E} + Q_{m,E} = 0 \quad (20)$$

270 where $Q_{f,E}$ and $Q_{m,E}$ are the energy sources/sinks for the fracture and matrix systems, $A_{f,E}$ is
 271 the energy per unit volume within the fracture expressed similarly to equation (17), $q_{f,E}$ is the
 272 energy flux within the fracture. However, by putting into consideration it obeys the theory of
 273 parallel plate for fracture opening. Expanding and solving for the sub-equations within (19) as
 274 presented in the matrix section of the heat transport (equation (15-18)) on fractures, yields the
 275 general expression for heat transport in fractures given in equation (20).

276

277 3. Finite element formulation for coupled TH model

278 This section presents the application of finite element method (FEM) to coupled TH problems
 279 in fully saturated and fractured porous media. The use of the coupled procedures and the partial
 280 differential equations (PDE) displayed above is incorporated in developing the FEM model. It
 281 is essential to define the initial and boundary conditions (BC) of the problem before
 282 formulating the finite element solutions. The initial conditions specify the field pressures and
 283 temperatures at $t=0$, i.e.

284
$$P=P_0, T=T_0 \text{ in } \Omega \text{ and on } \Gamma \quad (21)$$

285 where Ω is the domain of interest and Γ is the boundary.

286

287 In the case of BC's, they can be defined in two different kind that include the Dirichlet BC Γ
 288 , and the Neumann BC Γ^q . For the fluid flow, the Dirichlet pressure BC can be imposed as a
 289 constant value either at the injection/extraction wellbore boundaries, or far-field boundaries as

290
$$P=\hat{P} \text{ on } \Gamma_p \quad (22)$$

291 The Neumann BC for the fluid flow can be prescribed as a mass flux normal to the boundary
 292 surface or at the injection/extraction wellbore boundaries as

293
$$q_p = \rho_L \frac{\kappa}{\mu} (-\nabla P + \rho_L g \nabla z)^T \cdot n \text{ on } \Gamma_p^q \quad (23)$$

294 where n is normal to the boundary. Also, sometimes it can be employed as no-flow boundaries
 295 by setting equation (23) to zero.

296 In the case of heat transfer, the Dirichlet temperature BC can be imposed as a value (in the case
 297 of isothermal condition) at the injection wellbore boundary or far-field boundaries as

$$298 \quad T = \hat{T} \text{ on } \Gamma_T \quad (24)$$

299 The Neumann BC for the heat transfer can be imposed as a heat flux normal to a boundary or
 300 as an injection wellbore boundary (in the case of non-isothermal condition), which is given as

$$301 \quad q_T = (-\lambda \nabla T + \rho_L C_{p,L} v T)^T \cdot n \text{ on } \Gamma_T^q \quad (25)$$

302 In addition, the Neumann BC can also be prescribed as heat flux value at the heat outflow BC
 303 in the production wellbore boundary using the expression for the convective heat transfer as

$$304 \quad q_T = \rho_L v \cdot n.$$

305

306 The boundary value problem presented in the previous section, for example equations (8) is
 307 written as

$$308 \quad X(u) = B(u) + J = 0 \text{ in } \Omega \quad (26)$$

$$309 \quad Y(u) = D(u) + K = 0 \text{ on } \Gamma \quad (27)$$

310 where X and Y are the derivate of differential operators, B and D are appropriate differential
 311 operators, and J and K are known functions independent of the field variable u , which are the
 312 exact solution of the boundary value problem. By considering the integral statement

$$313 \quad \int_{\Omega} \varphi^T X(u) d\Omega + \int_{\Gamma} \hat{\varphi}^T Y(u) d\Gamma = 0 \quad (28)$$

314 is satisfied for a set of arbitrary functions φ and $\hat{\varphi}$, which is equivalent to satisfying differential
 315 equation (26) and (27). If equations (26) and (27) are satisfied, then equation (28) is true. An
 316 approximate solution is sought in the class of functions \hat{u} , namely

$$317 \quad u \approx \hat{u} = \sum_i^j N_i a_i = Na \quad (29)$$

318 which is obtained by introducing a set of trial or shape functions N_i regarding the coordinates;
 319 and a_i are the unknown values defined at points (nodes) in the domain Ω and the boundary
 320 Γ . If equation (29) is substituted into (26) and (27), they remain an error, or residual, i.e.

321
$$R = R_{\Omega} + R_{\Gamma} = X(\hat{u}) + Y(\hat{u}) \quad (30)$$

322 To minimise the residual over the whole domain and the boundary, a zero value for an
 323 appropriate number of integrals of the error over Ω and Γ , weighted by weighting functions w
 324 and \hat{w} , is sought, which is called the weighted residual method (WRM) [42], namely

325
$$\int_{\Omega} w^T X(\hat{u}) d\Omega + \int_{\Gamma} \hat{w}^T Y(\hat{u}) d\Gamma = 0 \quad (31)$$

326 Expression (31) is an approximation to the integral defined in equation (28) and results in a set
 327 of equations for the unknowns a_i , which can be written as

328
$$Ka = f \quad (32)$$

329 where K is the stiffness matrix, a is the unknown field; and f is the load matrix defined as

330
$$K_{ij} = \sum_{e=1}^m K_{ij}^e \quad f_i = \sum_{e=1}^m f_i^e \quad (33)$$

331 where K^e is known as the stiffness matrix for the e^{th} element and f^e is the boundary flux for
 332 the e^{th} element, and the derivative of the differential operators X and Y must be continuous
 333 over the domain. The WRM, that is equation (31), is now applied to mass conservation
 334 equations (8) and its Neumann boundary condition equation (21), which yields

335
$$\int_{\Omega} w^T \left\{ \nabla^T \left[\frac{\kappa}{\mu} (-\nabla P + \rho_L g \nabla z) \right] \right\} d\Omega + \int_{\Omega} w^T S \frac{\partial P}{\partial t} d\Omega + \int_{\Gamma_p^q} \hat{w}^T \left[\frac{\kappa}{\mu} (-\nabla P + \rho_L g \nabla z)^T \cdot n - \frac{q_p}{\rho_L} \right] \cdot d\Gamma = 0$$

 336
$$(34)$$

337 By limiting the choice of the weighting functions [42], such that

338
$$w = 0 \quad \text{on} \quad \Gamma_p \quad (35)$$

339
$$\hat{w} = -w \quad \text{on} \quad \Gamma_p^q \quad (36)$$

340 Applying the Green's theorem on the first portion of equation (34) and incorporating equations
 341 (35) and (36) into it, gives

342
$$\int_{\Omega} \left[-(w \nabla)^T \left(-\frac{\kappa}{\mu} \nabla P + \frac{\kappa}{\mu} \rho_L g \nabla z \right) \right] d\Omega + \int_{\Omega} w^T S \frac{\partial P}{\partial t} d\Omega + \int_{\Gamma_p^q} w^T \frac{q_p}{\rho_L} d\Gamma = 0 \quad (37)$$

343 The same procedure applied to the fluid flow when used in the energy balance equation in (18),
 344 and its Neumann boundary conditions in (24) by limiting the choice of weighting functions,
 345 such that

$$346 \quad w=0 \quad \text{on} \quad \Gamma_T \quad (38)$$

$$347 \quad \hat{w}=-w \quad \text{on} \quad \Gamma_T^q \quad (39)$$

348 also applying the Green's theorem to the second portion of equation (18), yields

$$349 \quad \int_{\Omega} w^T c_{\rho} \rho \frac{\partial T}{\partial t} d\Omega + \int_{\Omega} w \rho_L v c_{\rho,L} \cdot \nabla T d\Omega + \int_{\Omega} (\nabla w)^T \cdot (-\lambda \nabla T) d\Omega + \int_{\Gamma_T^q} w^T q^T d\Gamma = 0 \quad (40)$$

350 Equations (37) and (40) are the weak formulation (weak form) of the governing equations
 351 presented in section 2.2, and by applying the Galerkin FEM to discretise the weak form
 352 spatially [43]. The state variables are expressed regarding the nodal values and shape functions
 353 as

$$354 \quad P = N_p \hat{P} ; T = N_T \hat{T} \quad (41)$$

355 where \hat{P} and \hat{T} are the scalars of the nodal values of the pressures and temperature, N_p and
 356 N_T are shape functions. For a coarse tetrahedral element of 3D problem, they can be
 357 represented as

$$358 \quad N_p = [N_{p1} \ N_{p2} \ N_{p3} \ N_{p4}]^T, \ N_{pi} = \text{diagonal} \{N_{pi} \ N_{pi} \ N_{pi} \ N_{pi}\}, \ i=1,4$$

$$359 \quad (42)$$

$$360 \quad N_T = [N_{T1} \ N_{T2} \ N_{T3} \ N_{T4}]^T, \ N_{Ti} = \text{diagonal} \{N_{Ti} \ N_{Ti} \ N_{Ti} \ N_{Ti}\}, \ i=1,4 \quad (43)$$

361 By the introduction of equation (41) into equations (37) and (40); then applying the Galerkin
 362 FEM, and replacing the weighting functions w and \hat{w} with the corresponding shape functions
 363 N_p and N_T , gives

$$364 \quad \int_{\Omega} \left[(\nabla N_p)^T \frac{\kappa}{\mu} \nabla N_p \hat{P} - (\nabla N_p)^T \frac{\kappa}{\mu} \rho_L g \nabla z \right] d\Omega + \int_{\Omega} N_p^T S N_p \frac{\partial \hat{P}}{\partial t} d\Omega + \int_{\Gamma_T^q} N_p^T \frac{q_p}{\rho_L} d\Gamma = 0 \quad (44)$$

$$365 \quad \int_{\Omega} N_T^T c_{\rho} \rho N_T \frac{\partial \hat{T}}{\partial t} d\Omega + \int_{\Omega} \left[(N_T^T c_{\rho,L} q_m \cdot \nabla N_T) \hat{T} \right] d\Omega + \int_{\Omega} \nabla N_T^T (-\lambda \nabla N_T) \hat{T} d\Omega + \int_{\Gamma_T^q} N_T^T q^T d\Gamma = 0$$

$$366 \quad (45)$$

367 Further discretising equations (44) and (45) gives

$$368 \quad K_p = \int_{\Omega} N_p^T S N_p d\Omega \quad (46)$$

$$369 \quad M_p(T) = \int_{\Omega} (\nabla N_p)^T \frac{\kappa}{\mu} \nabla N_p d\Omega \quad (47)$$

$$370 \quad f^P(T) = \int_{\Omega} (\nabla N_p)^T \frac{\kappa}{\mu} \rho_L g d\Omega - \int_{\Gamma} N_p^T \frac{q_p}{\rho_L} d\Gamma \quad (48)$$

$$371 \quad K_T = \int_{\Omega} N_T^T c_{\rho} \rho N_T d\Omega \quad (49)$$

$$372 \quad M_T(P) = \int_{\Omega} \{N_T^T (\rho_L \nu c_{\rho,L} \cdot \nabla N_T) + \nabla N_T^T (-\lambda \nabla N_T)\} d\Omega \quad (50)$$

$$373 \quad f^T(P) = - \int_{\Gamma_f^g} N_T^T q_T d\Gamma \quad (51)$$

374 where K_p is the compressibility matrix; M_p is the permeability matrix; f^P is the load matrix
 375 for the fluid flow process; K_T is the capacity matrix; M_T is the conductivity matrix; and f^T
 376 is the load matrix for the heat transport. The staggered method is considered in coupling terms
 377 of the equations (44) and (45). By using equations (46) - (51), equations (44) and (45) are
 378 written as

$$379 \quad M_p(T) \hat{P} + K_p \frac{\partial \hat{P}}{\partial t} = f^P(T) \quad (52)$$

$$380 \quad M_T(P) \hat{T} + K_T \frac{\partial \hat{T}}{\partial t} = f^T(P) \quad (53)$$

381 The above equations are represented in matrix form as

$$382 \quad \begin{bmatrix} M_p(T) & 0 \\ 0 & M_T(P) \end{bmatrix} \begin{Bmatrix} \hat{P} \\ \hat{T} \end{Bmatrix} + \begin{bmatrix} K_p & 0 \\ 0 & K_T \end{bmatrix} \frac{\partial}{\partial t} \begin{Bmatrix} \hat{P} \\ \hat{T} \end{Bmatrix} = \begin{Bmatrix} f^P(T) \\ f^T(P) \end{Bmatrix} \quad (54)$$

383 Similarly, by applying the procedure of FEM solution obtained in (52) and (53) to the fracture
 384 equations in (14) and (20), yields

$$385 \quad M_{p,f}(T) \hat{P}_f + K_{p,f} \frac{\partial \hat{P}_f}{\partial t} = f^{P,f}(T) \quad (55)$$

$$M_{T,f}(P)\hat{T}_f + K_{T,f} \frac{\partial \hat{T}_f}{\partial t} = f^{T,f}(P) \quad (56)$$

where $K_{p,f}$ is the compressibility matrix for the fracture; $M_{p,f}$ is the permeability matrix for the fracture; $f^{p,f}$ is the load matrix for the fracture flow; $K_{T,f}$ is the capacity matrix for the fracture; $M_{T,f}$ is the conductivity matrix for the fracture; and $f^{T,f}$ is the load matrix for the fracture heat transport.

391

392 4. Solution procedure and verification

393 In this study, the fluid flow and the heat transport field equations are considered as independent
 394 systems for the pressure, and thermal multi-coupling mathematical model. The staggered
 395 method equation is used with the Galerkin method (finite element discrete method) in the
 396 geometry domain to obtain the numerical solution of the coupling iteration problems. Then, by
 397 applying the finite difference method (FDM) in the time domain as discussed in [44], to obtain
 398 the solution of the coupled equations (52) and (53), by

$$M_p(T)[P_{t+1} - P_t]/\Delta t + K_p[\theta P_{t+1} + (1-\theta)P_t] = f^p(T) \quad (57)$$

$$M_T(P)[T_{t+1} - T_t]/\Delta t + K_T[\theta T_{t+1} + (1-\theta)T_t] = f^T(P) \quad (58)$$

401 For the discrete fracture equations (55) and (56), the solution is obtained from

$$M_{p,f}(T)[P_{f,t+1} - P_{f,t}]/\Delta t + K_{p,f}[\theta P_{f,t+1} + (1-\theta)P_{f,t}] = f^{p,f}(T) \quad (59)$$

$$M_{T,f}(P)[T_{f,t+1} - T_{f,t}]/\Delta t + K_{T,f}[\theta T_{f,t+1} + (1-\theta)T_{f,t}] = f^{T,f}(P) \quad (60)$$

404 where t and $t+1$ indicates the previous and current time steps, respectively; Δt is the time
 405 step size; θ is the relaxation parameter with limit $0 \leq \theta \leq 1$. The FDM is employed to calculate
 406 parameter by time step, and the specified initial time step with an acceleration factor of 1. It is
 407 verified by repeated calculations to be stable and reliable for the computed results. The solution
 408 of the TH coupled nonlinear model is attained by using a mixture of Newton-Raphson and
 409 Picard schemes [45].

410

411 The convergence termination criterion employed for the nonlinear iterations in the study is the
 412 weighted Euclidean norm, which terminates the iteration solutions when the relative tolerance
 413 exceeds the relative error computed [46], given as

414

$$Error = \sqrt{\frac{1}{N_F} \sum_{j=1}^{N_F} \frac{1}{N_j} \sum_{i=1}^{N_j} \left(\frac{|E_{i,j}|}{W_{i,j}} \right)^2} \quad (61)$$

415

416

417

418

419

420

421

422

423

424

425

426

427

428

429

430

431

432

$$b = b_{\max} \sqrt{1 - x'^2} \quad (62)$$

433

434

435

436

437

438

439

440

441

442

where N_F is the number of fields and N_j is the number of degrees of freedom in field j . The double subscript denotes the degree of freedom index i and j component. E is the estimated error in the scalar, $W_{i,j} = \max(|U_{i,j}|, S_j)$, $U_{i,j}$ is the current approximation to the solution scalar, and S_j is a scale factor for which the program determines the scaling process.

To verify the solution capabilities described, a simple two-dimensional (2D) model is analysed by implementing the model in COMSOL with a link to MATLAB (COMMAT). The verification carried out here is the disturbance caused by the presence of fracture in a porous medium with a uniform flow. A similar problem was analysed by Strack as reported in [47], where an analytical model for this issue is derived as the potential flow. In this study, the model verified reported in [47] is used to verify the proposed model. Figure 2 presents the 2D model of the problem with a 1D fracture as a hydraulic conduit. Fluid is injected and extracted on the left P_{in} and right P_{out} sides of the model, respectively. On the other hand, the top and bottom represent no flow boundaries $\nabla P \cdot n = 0$. The fracture is 2 m in length with an orientation angle of 45° , and the flow is assumed to be laminar along its surface, and the shape is assumed to have normal displacements at the sides, as used in the case of a pressurised crack in an elastic medium, expressed as

where b_{\max} is the aperture at the centre and x' is the normalised local coordinate systems. Table 1[47] presents other parameters used in the numerical simulation of the porous media.

The results obtained are grouped into two sets. The first set of the results is the pressure distribution in the vicinity of the fracture and its flow pattern. Figure 3(a) presents the pressure distribution of the previously reported results [47], while Figure 3(b) depicts the numerical simulation carried out by the developed FE model. As observed, the results are in good agreement between the previous model and the FE model formulated in this work. The second set of the result verified in this study is the pressure profile along a diagonal line from the bottom-left passing through the fracture to the top-right of the geometry. Figure 4 presents the

443 results of both the previous work and the current FE model. As can be seen, the graph shows a
444 good agreement between the two solutions. Therefore, the capability of the newly developed
445 FE model is verified using a related problem applicable to porous medium modelling.

446

447 **5. Geothermal reservoir case study**

448 Figure 5(a), shows a schematic representation of the reservoir geometry for Soultz geothermal
449 system (i.e. half part of the reservoir), it depicts a deep geothermal system with $800\text{ m} \times 800$
450 $\text{m} \times 5000\text{ m}$ deep. The reservoir is assumed to be 300 m in thickness and is located at about
451 4.5 km below the ground surface, and bounded at top and bottom by impermeable layers of
452 granite. The top and bottom layers in Figure 5(a) represent the overburden and underburden,
453 and the middle layer in-between display the reservoir. The wellbores constitute a doublet
454 (single injector and producer) 11 m apart at the ground surface, and 600 m apart laterally at the
455 reservoir level as given in the Soultz geothermal system. Also, the injection well is positioned
456 100 m and 400 m in the horizontal and vertical distances, while the production well is located
457 700 m and 400 m in both the x and y coordinates as shown in Figure 5(a). Both the injector and
458 producer are inclined to angles of 10° and -10° , respectively.

459 Moreover, a single fracture intersects the reservoir through the overburden down to the
460 underburden layer as in Figure 5(a). The fracture dips at an angle of 60° , which is a normal
461 faulting regime to be precise with an approximated aperture of 50 mm.

462 Table 2 presents the petro-physical properties and physical parameters used in the
463 numerical model [4]. The material properties are extracted from the Soultz geothermal system
464 as in [4]. For the fluid material properties, expressions presented by Holzbecher [48] are
465 employed in the study, which includes density, viscosity, thermal conductivity, and heat
466 capacity. Details of the properties can be found [48]. The system at initial pressure is
467 hydrostatic throughout the model, and the initial temperature (T_{init}) is given as
468 $T_{init} = T_{surf} - 0.03[K/m] \times (-z)$, where T_{surf} is surface temperature and is assumed to be 283.15
469 K. The boundary condition applied for the temperature is 40°C (fluid injection temperature),
470 and for the hydraulic process is 30 l/s (injection flow rate). Moreover, explicit details of the
471 boundary conditions used in the geothermal reservoir model are provided in Table 3.

472

473 **5.1 Mesh and solution convergence**

474 In this model, the meshes are divided into three-dimensional (3-D) tetrahedral (for the matrix
475 block), two-dimensional (2-D) triangular (for the fracture), and one-dimensional (1-D) line

476 (wells) elements, respectively. Figure 5(b) showed the mesh system that connects finer and fine
477 grids in the calculation to reduce the impact of boundary effects. The implementation of the
478 finer meshes on the wellbores is to increase the calculation accuracy; and also strengthens the
479 calculating intensity and workload. Therefore, the mesh division method not only increases
480 calculation accuracy but also eradicate the deviation caused by inappropriately selected
481 boundary conditions, which have some significant effect on the long-term extracting vicinity
482 and heat recovery after extraction.

483 The mesh convergence study of the proposed geothermal reservoir has been examined
484 to explore the model computational efficiency in handling the cases of various structural
485 variations mentioned. Five mesh sizes are utilised: M1=20463, M2=39925, M3=68780,
486 M4=189774, and M5=747838 starting from coarse to extra fine. Figure 5(c) shows the results
487 representing temperature profiles along the production wellbore for all meshes. It is also
488 evident that there is no significant difference in the results between the five meshes, though the
489 results of the coarse and normal meshes, M1 and M2, are less accurate. However, it manifests
490 no numerical oscillations. Notwithstanding, it can be deduced that the model converged at M3
491 mesh. The CPU time for 55-time steps are M1=108 s, M2=201 s, M3=363 s, M4 = 1083 s, and
492 M5=10177 s in an Intel(R) Core(TM) i5-5200U CPU @ 2.20 GHz, 2 cores.

493 To overcome numerical errors in the FEM solution, it is essential to check the
494 convergence criterion for the solution. The convergence criterion in equation (58) is employed
495 for the error estimation during solution iterations for the geothermal reservoir modelling.
496 Figure 5(d) shows the number of iterations and the corresponding errors. The result indicates
497 that an average of five iterations is sufficient to obtain an accurate solution.

498

499 **5.2 Effect of cold water front**

500 For the matrix block, the analysis is performed with an injection rate of 20 l/s, an injection
501 temperature of 40°C, and a well lateral distance of 600 m. The temperature distribution study
502 confirms the activity of the coupled processes (between the thermal and hydraulic properties)
503 because the heat transfer mechanism is found to obey convective-dominated behaviour due to
504 the strong coupling. Figure 6(a) shows the temperature at time $t=0$, which happens to be same
505 as the initial temperature of the system, affirming that the effect of the Dirichlet BC is yet to
506 commence. However, there was a regional groundwater flow induced by the gradient from top
507 to bottom existing before the injection. Figure 6(b) shows temperature distribution results after
508 15 years of simulation, with some part of the matrix experiencing the cooling effect of the

509 injected fluid temperature. The process continues to propagate until the end of the simulation
510 (30 years), as shown in Figure 6(c).

511

512 To investigate the effect of cold water front in the reservoir, the cold water, at a temperature of
513 40°C, is injected at a rate of 20 l/s through two different injections well scenarios; one is
514 situated 100 m and the other 50 m away from the left end. Hot water is extracted by two
515 production wells; the first is located at 700 m, and the second at 750 m from the left end, as
516 shown in Figure 7(a-f). The effect of the cold water front propagation is examined after 1, 10
517 and 30 years of simulation for 600 m and 700 m lateral well spacing's as shown in Figures 7(a-
518 f). In all the cases analysed, it was observed that the injected fluid creates a cold front near the
519 injection well, which later evolves through the reservoir domain because the injected fluid is
520 cooler than the geothermal reservoir.

521 Also, it should be noticed that the temperatures of the right boundaries are kept equal
522 to the initial temperature of the reservoir until the cold-water front reaches the boundary, and
523 after that, the temperature of the boundary starts increasing as presented in Figures 7(c-f).

524

525 **5.3 Parametric studies**

526 Developing a design model efficient in assessing the lifespan of a geothermal reservoir requires
527 the understanding of some key control parameters during exploration and exploitation. In this
528 study, three basic human control parameters are analysed by varying one parameter at a time
529 using the OFAT approach, while keeping the rest at a constant based on the Soultz geothermal
530 case, as presented in Section 5.1. The human control parameters studied here are injection flow
531 rate (discharge), injection fluid temperature, and lateral well spacing. Studying these three key
532 parameters provides a preliminary evaluation of the effects of reservoir parameters on the
533 commercial applicability of enhanced geothermal system utilisation. The effects of the
534 parameters are assessed based on the productivity of the reservoir during the exploitation period
535 of 30 years. The geothermal reservoir conditions specified are simulated to acquire the
536 anticipated variations in temperature, pressure, and thermal energy over 30 years. The
537 parameters studied vary over the range of values that are acceptable for the geothermal
538 exploitation of the Soultz site.

539 In a nutshell, the temperature of the reservoir was monitored using the parameters given
540 above at production wellhead with a simulation period of 30 years.

541

542 **5.3.1 Effect of injection flow rate**

543 The injection flow rate is one of the human control parameters that have a direct effect on the
544 reservoir lifespan. In order to quantify the effect, six cases were analysed. These cases range
545 from 20 to 70 l/s with an incremental step of 10 l/s. Each of the cases is then studied under
546 different scenarios of injection temperature and well separation distances of 40°C and 50°C,
547 and 600 and 700 m, respectively. All other parameters remain constant as explained before.
548 Figure 8 shows the production wellbore temperature curves for the effect of various injection
549 flow rates. Figures 8(a) and 8(b) present the temperature history at the production well for the
550 scenarios of 40°C and 50°C under the effect of 600 m well distance, while Figures 8(c) and
551 8(d) show the production temperature for the same scenarios of injection temperature above
552 with 700 m well spacing.

553 Figure 8a shows the temperature curves at the production wellbore for the different
554 injection flow rates under a constant injection temperature of 40°C and lateral well spacing of
555 600 m. As seen, the temperature curves differ for the various cases; the higher rate declines
556 earlier than the lower rate. For example, the 70 l/s injection flow rate starts to decline just after
557 0.8 years of simulation, whereas the 20 l/s injection flow rate begins to decrease after
558 approximately 2.6 years. As a result, the produced temperature is higher when the injection
559 flow rate is lower, and vice versa. The reason for the variation is that the greater the injection
560 flow rate, the faster the cooling of the reservoir is, and the lower the flow rate, the slower the
561 cooling becomes. The same trend is observed in Figure 8b when the injection fluid temperature
562 is changed to 50°C in similar operational scenarios as in Figure 8a, with slight shifts in the
563 production temperature. It is noted that the increase in the injection fluid temperature to 50°C
564 has a lesser effect on the produced temperature in those cases.

565 Figure 8c presents the temperature breakthrough curves at the production well for
566 different injection flow rates under the influence of 40°C injection temperature and 700 m
567 lateral well spacing. In these cases, the earliest decline starts after 1.6 years of simulation for
568 the highest injection rate (i.e. 70 l/s) and 5.6 years in the case of lowest injection flow rate (20
569 l/s). Furthermore, the decrease in the production temperature at the extraction well during the
570 30-year simulation is 8.31°C and 8.93°C for the lowest and highest injection flow rates,
571 respectively. The low decline is recorded in these cases because the lateral well spacing
572 between the injector and the producer is larger, so the production well bore is not affected much
573 by the reservoir cooling after a 30-year simulation. Likewise, the same response is observed in
574 Figure 8d with slight changes in the production temperature due to the increase in the injection
575 fluid temperature.

576 In all the cases and scenarios, it is observed that as the injection rate increases, the reservoir
577 temperature decreases rapidly. Moreover, the injection temperature and the well spacing also
578 have some effects on the production rate. The maximum temperature is achieved when the
579 injection temperature is at its lowest and well spacing is at its largest, then combined with the
580 lower injection rate as shown in the figures presented.

581

582 5.3.2 Effect of injection fluid temperature

583 The surrounding rock supplies some amount of the heat enthalpy conducted in the reservoir;
584 however, the injected fluid temperature governs the major heat enthalpy added into the
585 reservoir due to the convective heat transfer. In this study, six cases of fluid injection
586 temperature are investigated. These cases range from 10°C to 60°C with an incremental step
587 of 10°C, and each of the cases is additionally studied under varying scenarios of pumping rates
588 of 20 l/s and 30 l/s, and well lateral spacing of 600 m and 700 m. Figure 9 shows the temperature
589 production curves for the effect of injection fluid temperatures. Figures 9(a) and 9(b) present
590 the produced temperature for the scenarios of 20 l/s and 30 l/s following the influence of 600
591 m well spacing. Figure 9a shows the breakthrough temperature curves at the production well;
592 the temperature curves begin to decline after approximately 1.8 years of simulation with a
593 temperature of 150.93°C in almost all cases. After approximately 10-12 years of simulation, a
594 little gap is observed between the different injection temperature scenarios, and it continues to
595 widen till the 30-year simulation period. The reason for these similarities in the production
596 temperature breakthrough curves is that the effect of reservoir cooling started in approximately
597 the same period in all cases. Similarly, Figure 9b shows the production breakthrough curves
598 for the different injection temperature scenarios when combined with 30 l/s injection flow rate
599 and 600 m lateral well spacing. As can be seen, the production temperature trend is similar to
600 Figure 9a with little difference; in this case, the decline started after approximately 1.2 years
601 of simulation (earlier than the former scenario) with a temperature of 150.93°C in almost all
602 cases. Also, in this scenario, some little deviations are seen from approximately 8.5-10 years,
603 and these continue to grow until the end of the simulation. The idea behind the earlier variation
604 between the different cases is the increase in the injection flow rate to 30 l/s, which causes the
605 fast cooling of the reservoir.

606 Similarly, Figures 9(c) and 9(d) show the production temperatures using the same
607 injected rate with 700 m well spacing. Figure 9c shows the temperature curves at the production
608 wellbore for different cases of the injection fluid temperature under the influences of 20 l/s
609 injection flow rate and 700 m lateral well spacing. As seen, the temperature breakthrough

610 curves have a similar trend except in the case of the 10°C injection fluid temperature rate. The
611 production temperature began to decline after approximately 4.2 years of the simulation cases
612 of 20°C to 60°C, while in the case of the 10°C injection scenario, it began at approximately
613 three years of simulation. The temperatures at the decline stages are 150.73°C and 150.74°C,
614 in both the former and the latter, respectively. As the simulation continues, the breakthrough
615 curve for the 10°C injection cases shows a sudden transition change from lower to higher
616 between 8.8 and 9.2 simulation period and maintains a regular pattern till the end of the
617 simulation, whereas the other cases maintain the same decline pattern. The reason for the
618 variation of the 10°C case with remaining scenarios is that after equilibrium is reached for
619 cooling the higher injection rate propagates faster to the production wellbore than the former.
620 Likewise, Figure 9d shows similar breakthrough curves as in Figure 9c with little difference
621 concerning the starting period of decline and the transition phases of the 10°C injection due to
622 the increase in the injection flow rate. Apart from those points, all other trend remains the same.
623 In all the scenarios studied, it is observed that there were no significant changes in the produced
624 temperature from the reservoir.

625

626 5.3.3 Effect of lateral well spacing

627 To overcome the cold water effect and water losses that result from reduced productivity of
628 reservoir wells, they must be placed at an optimum distance from each other. The choice of
629 place will depend on the geological formation and production flow rates. Larger well spacing
630 results in greater reservoir sizes and vice versa. However, with large spaces between wells,
631 fluid losses are likely to be a significant problem, and with small spaces, the fluid losses are
632 negligible. Therefore, the well spacing must be optimised to achieve the maximum possible
633 reservoir size and production flow rate. In this work, six scenarios of well lateral spacing are
634 examined. The spaces between the reservoir wells are chosen as 400, 500, 600, 650, 700, and
635 750 metres long, respectively. Also, in each of the scenarios, different injection rates, of 20 l/s
636 and 30 l/s, and injection fluid temperatures, of 30°C and 40°C, are analysed. Figure 10 presents
637 the temperature curve at the production wellbore for the effect of lateral well spacing. Figures
638 10(a) and 10(b) show the produced temperature in the cases where 20 l/s were injected at 30°C
639 and 40°C, respectively while Figures 10(c) and 10(d) show the production temperature when
640 30 l/s were injected at 30°C and 40°C respectively.

641 Figure 10a shows the temperature breakthrough curve at the extraction well for the
642 different scenarios of the lateral well spacing when combined with an injection fluid
643 temperature of 30°C and injection flow rate of 20 l/s. As can be seen, the further the spacing,

644 the higher the produced temperature, and vice versa. For instance, in the case of 400 m lateral
 645 well spacing, the temperature begins to decrease just after 0.8 years of the simulation period.
 646 Concerning the 700 m lateral wellbore spacing, the decline starts after approximately 9.4 years.
 647 Moreover, after a simulation period of 30 years, the produced temperature for the closer well
 648 spacing (i.e., 400 m) was approximately 116°C, and the largest spacing (750 m) is 145°C,
 649 which amounted to a 30°C temperature difference between the two cases. The reason for this
 650 significant deviation between the scenarios is the closer the spacing, the higher the impact of
 651 cold water propagation on the production wellbore, and vice versa. Likewise, a similar trend
 652 of Figure 10a is seen in Figures 10b-d, with slight sights in the temperature breakthrough curves
 653 due to the different injection fluid temperatures and flow rates employed.

654 In all the scenarios, it is observed that as the lateral well spacing increases, the
 655 production temperature rises.

656

657 **5.4 Energy extraction rates**

658 The model adopted in this investigation is the one proposed by Kruger [49][50] for the
 659 calculations of the total energy extraction in all the scenarios and cases, expressed here as

$$660 \quad \Delta E_i = Q_i C_{\rho,L} \Delta T_i \quad (63)$$

661 where ΔE_i is the annual energy produced in the i^{th} year, Q_i is the total production flowrate
 662 in the i^{th} year, $C_{\rho,L}$ is the specific heat capacity of the circulated fluid, and ΔT_i is the
 663 temperature difference between the extracted and injected fluid in the i^{th} year. The total energy
 664 produced from the system for 30 years of extraction can be written as

$$665 \quad \Delta E = \sum_{i=1}^{30} \Delta E_i \quad (64)$$

666

667 Based on the limitations of the injection flow rate range and other parameter combinations
 668 studied in this work using the OFAT approach, the results show that as the injection flow rate
 669 increases, the energy extraction rate increases with a positive linear relationship as indicated in
 670 Figure 11, which shows that the injection rate increase affects the production output. Figure 11
 671 also shows the influence of well spacing and the effect of injection fluid temperature on the
 672 energy extraction rate when combined with injection scenarios. The results revealed that wider

673 well spacing coupled with lower fluid injection temperatures yields higher energy when
674 compared to larger spacing with higher rates.

675

676 As for the effect of fluid injection temperature on the energy extraction rate, Figure 12 shows
677 an inverse relationship between fluid injection temperature and the energy extraction rate. As
678 the fluid injection temperature rises, the energy extracted from the reservoir declines
679 significantly, because ΔT_i reduces with the rising fluid injection temperature. Hence, the
680 reservoir lifespan is prolonged for the reproduction of hot water with the same temperature.
681 Also, these cases are further investigated with different well spacing and fluid injection rates,
682 and the results showed that larger well spacing linked with a higher injection fluid rate
683 generates greater extraction energy in comparison to other combinations.

684

685 Figure 13 presents the effect of well spacing on the extraction energy of the reservoir. In all the
686 scenarios analysed, it is observed that, as the well spacing increased, the energy extracted from
687 the system increases rapidly due to the cold water front propagation affecting the closer wells
688 earlier than the further ones. The increase shown in Figure 13 occurs in a nonlinear manner
689 with two different gradients; the gradient of the first two spacing is steeper than the remaining
690 ones because the latter spacing have similar resistance to the cold water front.

691

692 **6. Conclusions**

693 In this paper, a three-dimensional numerical model for coupled thermo-hydraulic processes in
694 a heterogeneous fractured geothermal reservoir overlain and underlain by impermeable layers
695 is proposed. The primary objective is to examine the effect of human control parameters on
696 geothermal reservoir productivity. A verification study is first performed to test the capability
697 of the solver, and the outcomes achieved are in agreement with the existing solvers. Also
698 presented in the studies is the effect of cold water in the matrix block and reservoirs before
699 conducting the main analyses on the human control parameters. An extensive parametric
700 analysis is investigated for a broad range of the parameters and operational scenarios. The
701 injection flow rate has a significant effect on energy production as the rate increases, the energy
702 extraction rate rises, and the system lifetime decreases. Thus, higher injection flow rate is a
703 positive factor in production and, at the same time, a negative factor on reservoir lifespan. In
704 the case of fluid injection temperature, the effect is less significant to production because, as
705 the injection temperature increases, the extraction energy declines rapidly and the reservoir

706 lifespan increases. The well lateral spacing also behaves similarly to the injection flow rate,
707 but it is not as effective as the injection flow rate regarding energy extraction and provides a
708 longer reservoir lifetime than the former.

709 The developed model gives in-depth insight to stakeholders and reservoir engineers
710 with regard to the key parameters to control during exploration and exploitation. The results
711 presented can be effectively employed in the design of human control parameters in a
712 geothermal reservoir system. The model can also serve as a reference solution to other complex
713 interactions encountered in reservoir simulations.

714

715 **Acknowledgement**

716 The first author delightedly acknowledges the PhD scholarship funding support received from
717 both the University of Greenwich (UK) and the Petroleum Technology Development Fund
718 (PTDF) (Nigeria).

719

720 **References**

- 721 [1] A. H. D. Cheng, A. Ghassemi, and E. Detournay, "Integral equation solution of heat
722 extraction from a fracture in hot dry rock," *Int. J. Numer. Anal. Methods Geomech.*,
723 vol. 25, no. 13, pp. 1327–1338, 2001.
- 724 [2] A. Ghassemi, S. Tarasovs, and A. H.-D. Cheng, "A 3-D study of the effects of
725 thermomechanical loads on fracture slip in enhanced geothermal reservoirs," *Int. J.*
726 *Rock Mech. Min. Sci.*, vol. 44, no. 8, pp. 1132–1148, Dec. 2007.
- 727 [3] O. Kolditz, "Modelling flow and heat transfer in fractured rocks: Conceptual model of
728 a 3-D deterministic fracture network," *Geothermics*, vol. 24, no. 3, pp. 451–470, Jun.
729 1995.
- 730 [4] M. D. Aliyu and H. Chen, "Numerical Modelling of Coupled Hydro-Thermal
731 Processes of the Soultz Heterogeneous Geothermal System," in *ECCOMAS Congress*
732 *2016 VII European Congress on Computational Methods in Applied Sciences and*
733 *Engineering M. Papadrakakis, V. Papadopoulos, G. Stefanou, V. Plevris (eds.) Crete*
734 *Island, Greece, 5–10 June 2016*, 2016, no. Volume I, pp. 1659–1671.
- 735 [5] J. Willis-Richards and T. Wallroth, "Approaches to the modelling of HDR reservoirs: A
736 review," *Geothermics*, vol. 24, no. 3, pp. 307–332, Jun. 1995.
- 737 [6] A. E. Croucher and M. J. O'Sullivan, "Application of the computer code TOUGH2 to
738 the simulation of supercritical conditions in geothermal systems," *Geothermics*, vol.
739 37, no. 6, pp. 622–634, 2008.

- 740 [7] M. J. O’Sullivan, K. Pruess, and M. J. Lippmann, “State of the art of geothermal
741 reservoir simulation,” *Geothermics*, vol. 30, no. 4, pp. 395–429, Aug. 2001.
- 742 [8] M. J. O’Sullivan, A. Yeh, and W. I. Mannington, “A history of numerical modelling of
743 the Wairakei geothermal field,” *Geothermics*, vol. 38, no. 1, pp. 155–168, Mar. 2009.
- 744 [9] M. J. O’Sullivan, K. Pruess, and M. J. Lippmann, “Geothermal Reservoir Simulation :
745 the State-of-Practice and Emerging Trends,” in *World Geothermal Congress 2000,*
746 *Kyushu - Tohoku, Japan, May 28 - June 10, 2000*, 2000, pp. 4065–4070.
- 747 [10] H. Xing, Y. Liu, J. Gao, and S. Chen, “Recent development in numerical simulation of
748 enhanced geothermal reservoirs,” *J. Earth Sci.*, vol. 26, no. 1, pp. 28–36, 2015.
- 749 [11] Z. Y. Wong, R. Horne, and D. Voskov, “Comparison of Nonlinear Formulations for
750 Geothermal Reservoir Simulations,” in *41st Workshop on Geothermal Reservoir*
751 *Engineering, Stanford, 2016*, no. 2011, pp. 1–16.
- 752 [12] Y. Xia, M. Plummer, R. Podgorney, and A. Ghassemi, “An Assessment of Some
753 Design Constraints on Heat Production of a 3D Conceptual EGS Model Using an
754 Open-Source Geothermal Reservoir Simulation Code,” in *Stanford Geothermal*
755 *Workshop, 2016*, pp. 1–24.
- 756 [13] M. G. Blöcher, G. Zimmermann, I. Moeck, W. Brandt, A. Hassanzadegan, and F.
757 Magri, “3D numerical modeling of hydrothermal processes during the lifetime of a
758 deep geothermal reservoir,” *Geofluids*, vol. 10, no. 3, pp. 406–421, 2010.
- 759 [14] T. Fischer, D. Naumov, S. Sattler, O. Kolditz, and M. Walther, “GO2OGS 1.0: A
760 versatile workflow to integrate complex geological information with fault data into
761 numerical simulation models,” *Geosci. Model Dev.*, vol. 8, no. 11, pp. 3681–3694,
762 2015.
- 763 [15] E. Wall, “United States Geothermal Support and the International Partnership for
764 Geothermal Technology,” in *World Geothermal Congress 2010 Bali, Indonesia, 25-29*
765 *April 2010*, 2010, no. April, pp. 1–4.
- 766 [16] S. K. White, S. Purohit, and L. Boyd, “Using GTO-Velo to Facilitate Communication
767 and Sharing of Simulation Results in Support of the Geothermal Technologies Office
768 Code Comparison Study,” in *Fourtieth Workshop on Geothermal Reservoir*
769 *Engineering, 2015*, pp. 1–10.
- 770 [17] M. D. White and B. R. Phillips, “Code Comparison Study Fosters Confidence in the
771 Numerical Simulation of Enhanced Geothermal Systems,” in *40th Stanford*
772 *Geothermal Workshop, 2015*, pp. 1–12.
- 773 [18] A. Ghassemi, S. Kelkar, and M. McClure, “Influence of Fracture Shearing on Fluid

- 774 Flow and Thermal Behavior of an EGS Reservoir - Geothermal Code Comparison
775 Study,” in *Fourtieth Workshop on Geothermal Reservoir Engineering*, 2015, pp. 1–14.
- 776 [19] J. Burnell, M. O. Sullivan, J. O. Sullivan, W. Kissling, A. Croucher, J. Pogacnik, G.
777 Caldwell, S. Ellis, S. Zarrouk, and M. Climo, “Geothermal Supermodels : the Next
778 Generation of Integrated Geophysical , Chemical and Flow Simulation Modelling
779 Tools,” in *Proceedings World Geothermal Congress 2015 Melbourne, Australia, 19-
780 25 April 2015*, 2015, no. April, pp. 19–25.
- 781 [20] T. H. Fairs, P. L. Younger, and G. Parkin, “Parsimonious numerical modelling of deep
782 geothermal reservoirs,” in *Proceedings of the Institution of Civil Engineers, Energy*,
783 2015, pp. 1–11.
- 784 [21] M. Shook, “Parametric Study o f Reservoir Properties and Their Effect on Energy
785 Recovery The Effect of Reservoir Structure,” in *Geothermal Reservoir Engineering
786 Stanford University*, 1992, pp. 63–71.
- 787 [22] G. Nalla, G. M. Shook, G. L. Mines, and K. K. Bloomfield, “Parametric sensitivity
788 study of operating and design variables in wellbore heat exchangers,” *Geothermics*,
789 vol. 34, no. 3, pp. 330–346, 2005.
- 790 [23] A. Vecchiarelli, R. Sousa, and H. H. Einstein, “PARAMETRIC STUDY WITH
791 GEOFRAC: A THREE-DIMENSIONAL STOCHASTIC FRACTURE FLOW
792 MODEL,” in *Thirty-Eighth Workshop on Geothermal Reservoir Engineering Stanford
793 University, Stanford, California, February 11-13, 2013 SGP-TR-198*, 2013, no. 1992,
794 pp. 1–9.
- 795 [24] J. Chen and F. Jiang, “Designing multi-well layout for enhanced geothermal system to
796 better exploit hot dry rock geothermal energy,” *Renew. Energy*, vol. 74, pp. 37–48,
797 2015.
- 798 [25] C. Jain, C. Vogt, and C. Clauser, “Maximum potential for geothermal power in
799 Germany based on engineered geothermal systems,” *Geotherm. Energy*, vol. 3, no. 1,
800 p. 15, 2015.
- 801 [26] S. E. Poulsen, N. Balling, and S. B. Nielsen, “A parametric study of the thermal
802 recharge of low enthalpy geothermal reservoirs,” *Geothermics*, vol. 53, pp. 464–478,
803 2015.
- 804 [27] M. D. Aliyu, H. Chen, and O. Harireche, “Finite element modelling for productivity of
805 geothermal reservoirs via extraction well,” in *Proceedings of the 24th UK Conference
806 of the Association for Computational Mechanics in Engineering 31 March– 01 April
807 2016, Cardiff University, Cardiff*, 2016, no. April, pp. 331–334.

- 808 [28] G. B. Madhur and J. B. Anderson, “Sensitivity Analysis of Low-Temperature
809 Geothermal Reservoirs: Effect of Reservoir Parameters on the Direct Use of
810 Geothermal Energy,” *GRC Trans.*, vol. 36, no. 10, pp. 1255–1262, 2012.
- 811 [29] S. Saeid, R. Al-Khoury, H. M. Nick, and M. A. Hicks, “A prototype design model for
812 deep low-enthalpy hydrothermal systems,” *Renew. Energy*, vol. 77, pp. 408–422,
813 2015.
- 814 [30] R. Hebert and B. Ledesert, “Calcimetry at soultz-sous-forêts enhanced geothermal
815 system: relationships with fracture zones, flow pathways and reservoir chemical
816 stimulation results,” in *In “Geothermal Energy, Technology and Geology”, Edited by
817 Jianwen Yang, Nova Science Publishers Inc., NY, Chapter 3*, no. September 2016, J.
818 Yang, Ed. Nova Science Publishers, Inc., 2012, pp. 93–113.
- 819 [31] R. L. Hébert, B. Ledésert, D. Bartier, C. Dezayes, A. Genter, and C. Grall, “The
820 Enhanced Geothermal System of Soultz-sous-Forêts: A study of the relationships
821 between fracture zones and calcite content,” *J. Volcanol. Geotherm. Res.*, vol. 196, no.
822 1–2, pp. 126–133, Sep. 2010.
- 823 [32] D. W. Brown, “Hot dry rock geothermal energy: important lessons from Fenton Hill,”
824 in *Thirty-Fourth Workshop on Geothermal Reservoir Engineering*, 2009, pp. 3–6.
- 825 [33] M. D. Aliyu and H.-P. Chen, “Sensitivity analysis of deep geothermal reservoir: Effect
826 of reservoir parameters on production temperature,” *Energy*, vol. 129, pp. 101–113,
827 Jun. 2017.
- 828 [34] K. J. Bathe, H. Zhang, and M. H. Wang, “Finite element analysis of incompressible
829 and compressible fluid flows with free surfaces and structural interactions,” *Comput.
830 Struct.*, vol. 56, no. 2–3, pp. 193–213, Jul. 1995.
- 831 [35] C.-F. Tsang, “Linking Thermal, Hydrological, and Mechanical Processes in Fractured
832 Rocks,” *Annu. Rev. Earth Planet. Sci.*, vol. 27, no. 1, pp. 359–384, May 1999.
- 833 [36] R. W. Zimmerman, “Coupling in poroelasticity and thermoelasticity,” *Int. J. Rock
834 Mech. Min. Sci.*, vol. 37, no. 1–2, pp. 79–87, 2000.
- 835 [37] Z. Chen, G. Huan, and Y. Ma, *Computational Methods for Multiphase Flows in
836 Porous Media*, 1st ed. Philadelphia: Society for Industrial and Applied Mathematics,
837 2006.
- 838 [38] J. Warren and P. J. Root, “The behavior of naturally fractured reservoirs,” *SPE J.*, vol.
839 3, no. 3, pp. 245–255, 1963.
- 840 [39] G. . Barenblatt, I. . Zheltov, and I. . Kochina, “Basic concepts in the theory of seepage
841 of homogeneous liquids in fissured rocks [strata],” *J. Appl. Math. Mech.*, vol. 24, no. 5,

842 pp. 1286–1303, Jan. 1960.

843 [40] T. Arbogast, J. Douglas, Jr., and U. Hornung, “Derivation of the Double Porosity
844 Model of Single Phase Flow via Homogenization Theory,” *SIAM J. Math. Anal.*, vol.
845 21, no. 4, pp. 823–836, 1990.

846 [41] K. M. Bower and G. Zyvoloski, “A numerical model for thermo-hydro-mechanical
847 coupling in fractured rock,” *Int. J. Rock Mech. Min. Sci.*, vol. 34, no. 8, pp. 1201–
848 1211, Dec. 1997.

849 [42] R. W. Lewis, P. Nithiarasu, and K. N. Seetharamu, *Fundamentals of the Finite
850 Element Method for Heat and Fluid Flow*. Chichester, UK: John Wiley & Sons, Ltd,
851 2005.

852 [43] H. Fan and S. Li, “A three-dimensional surface stress tensor formulation for simulation
853 of adhesive contact in finite deformation,” *Int. J. Numer. Methods Eng.*, vol. 107, no.
854 3, pp. 252–270, Jul. 2016.

855 [44] M. Ferronato, N. Castelletto, and G. Gambolati, “A fully coupled 3-D mixed finite
856 element model of Biot consolidation,” *J. Comput. Phys.*, vol. 229, no. 12, pp. 4813–
857 4830, 2010.

858 [45] F. Auricchio, A. Lefieux, A. Reali, and A. Veneziani, “A locally anisotropic fluid-
859 structure interaction remeshing strategy for thin structures with application to a hinged
860 rigid leaflet,” *Int. J. Numer. Methods Eng.*, vol. 107, no. 2, pp. 155–180, Jul. 2016.

861 [46] COMSOL, “COMSOL Reference Manual,” CM020005, 2015.

862 [47] O. Kolditz, U.-J. Görke, H. Shao, and W. Wang, *Thermo-Hydro-Mechanical-Chemical
863 Processes in Porous Media: Benchmarks and Examples*, vol. 86. Berlin, Heidelberg:
864 Springer Berlin Heidelberg, 2012.

865 [48] E. O. Holzbecher, *Modeling Density-Driven Flow in Porous Media*. Berlin,
866 Heidelberg: Springer Berlin Heidelberg, 1998.

867 [49] P. Kruger, “HEAT EXTRACTION FROM HDR GEOTHERMAL RESERVOIRS,” in
868 *World Geothermal Congress, 1995: Florence, Italy, 18-31 May 1995*, 1995, no. C, pp.
869 2517–2520.

870 [50] Y. Xia, M. Plummer, E. Mattson, R. Podgorney, and A. Ghassemi, “Design, modeling,
871 and evaluation of a doublet heat extraction model in enhanced geothermal systems,”
872 *Renew. Energy*, vol. 105, pp. 232–247, 2017.

873

874
875
876
877
878
879

Table 1: Model parameters adopted in model verification [42]

Parameters	Symbol	Value	Unit
Porosity	ϕ	1	%
Hydraulic conductivity	K	1 e-5	m/s
Fracture hydraulic conductivity	K_f	1 e-3	m/s
Specific storage	S	1 e-4	m/s
Injection pressure	P_{in}	4.965 e+5	Pa
Extraction pressure	P_{out}	-4.965 e+5	Pa
Density	ρ	1,000	kg/m ³
Viscosity	μ	0.001	Pa.s

880
881

882

883

884

Table 2: Geological and petro-physical properties of the system [4]

Parameter	Symbol	Value	Unit
Overburden Layer			
Thermal conductivity	λ_s	2	W/m/K
Density	ρ_s	2500	Kg/m ³
Heat capacity	$C_{\rho,S}$	900	J/kg/K
Porosity	ϕ	0.1	1
Permeability	κ	1 e-18	m ²
Reservoir			
Thermal conductivity	λ_s	3	W/m/K
Density	ρ_s	2650	Kg/m ³
Heat capacity	$C_{\rho,S}$	850	J/kg/K
Porosity	ϕ	0.3	1
Permeability	κ	1 e-16	m ²
Underburden Layer			
Thermal conductivity	λ_s	3.5	W/m/K
Density	ρ_s	2700	Kg/m ³
Heat capacity	$C_{\rho,S}$	850	J/kg/K
Porosity	ϕ	0.3	1
Permeability	κ	1 e-18	m ²
Fracture			
Thermal conductivity	$\lambda_{f,s}$	3.5	W/m/K
Density	$\rho_{f,s}$	1200	Kg/m ³
Heat capacity	$C_{\rho,S}$	800	J/kg/K
Porosity	ϕ_f	0.01	1
Permeability	κ_f	1 e-12	m ²

885

886

887

888

889

890

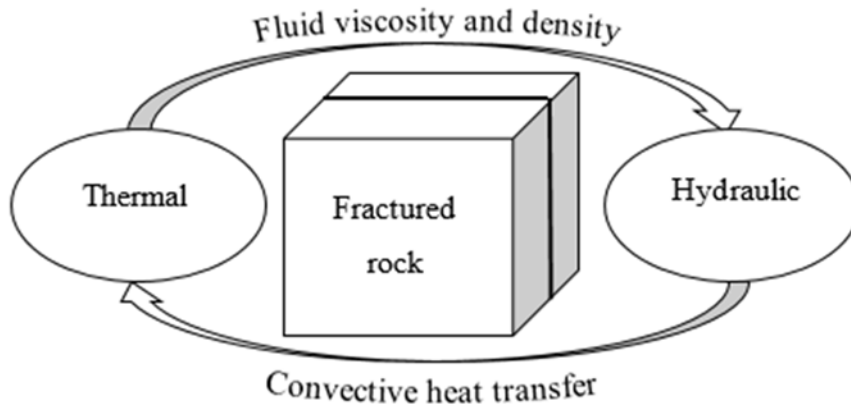
Table 3: The boundary conditions employed in the geothermal reservoir model

Physics	Boundary reference	Boundary condition
Hydraulic	Injection wellbore (i.e. injection flow rate)	$Q(t)_{injection} = 30 \text{ l/s}$ $0 \leq t \leq 30$
	Production wellbore (i.e. production flow rate)	$Q(t)_{production} = -30 \text{ l/s}$ $0 \leq t \leq 30$
	Surfaces (top & bottom) except at the injection and production areas.	$Q(t) = 0$ $0 \leq t \leq 30$
	Surfaces (front, back, left, and right).	$P(t) = \rho_L g (H_0 - D)$, i.e., $-\partial H \times x$ $0 \leq t \leq 30$
Thermal	Injection wellbore (i.e. injection temperature)	$T(t)_{injection} = 40^\circ\text{C}$ $0 \leq t \leq 30$
	Production wellbore (i.e. unknown temperature to be calculated)	$T(t)_{production} = ?$ $0 \leq t \leq 30$
	Surfaces (top & bottom) except at the injection and production areas. In this case, the boundaries are thermal insulated.	$-n \cdot q(t) = 0$ $0 \leq t \leq 30$
	Surfaces (front, back, left, and right).	$T(t) = T_{init}(t)$ if $n \cdot v < 0$, $-n \cdot q(t) = 0$, if $n \cdot v \geq 0$, $0 \leq t \leq 30$

891

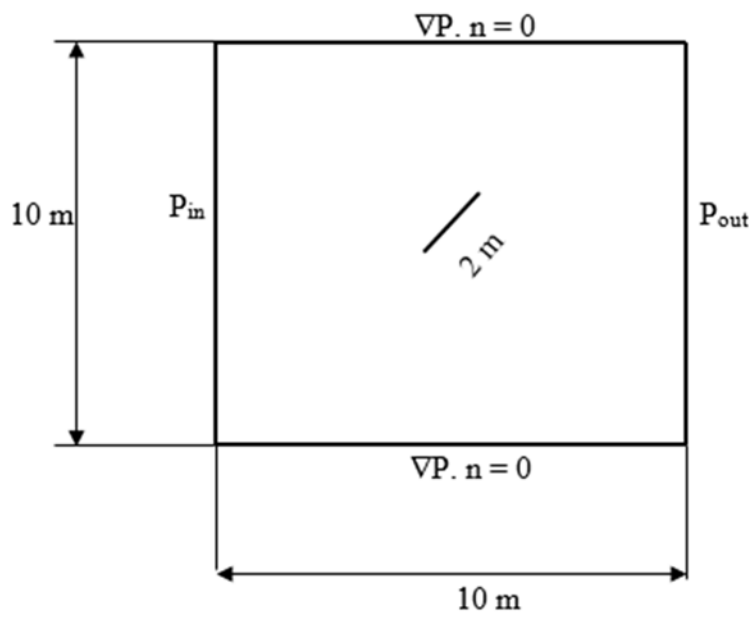
892

893
894
895



896
897
898
899

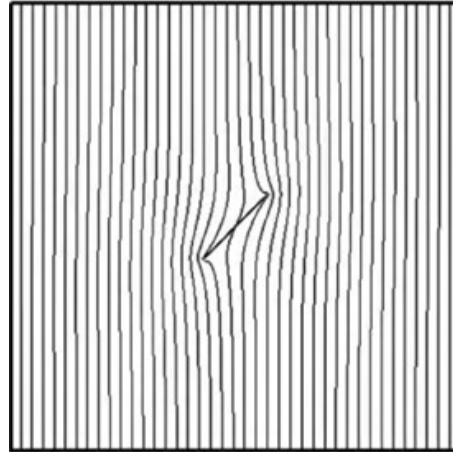
Figure 1: Two-way fully coupled Thermo-Hydro model



900
901
902

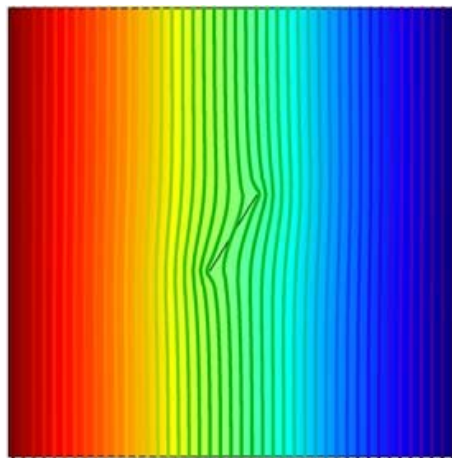
Figure 2: Model set-up (After [42])

903
904
905
906
907



908
909
910

Figure 3(a): Pressure distribution in [42]

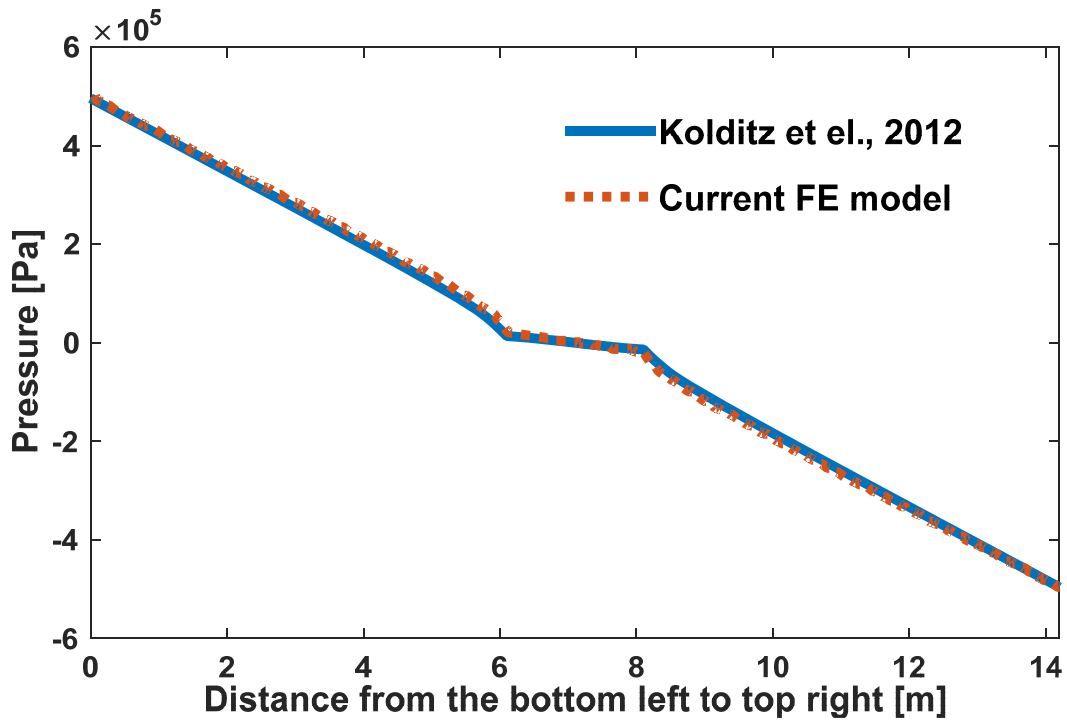


911
912
913
914

Figure 3(b): Pressure distribution for the current FE model

Figure 3: Verification of the proposed procedure with the existing model in [42]

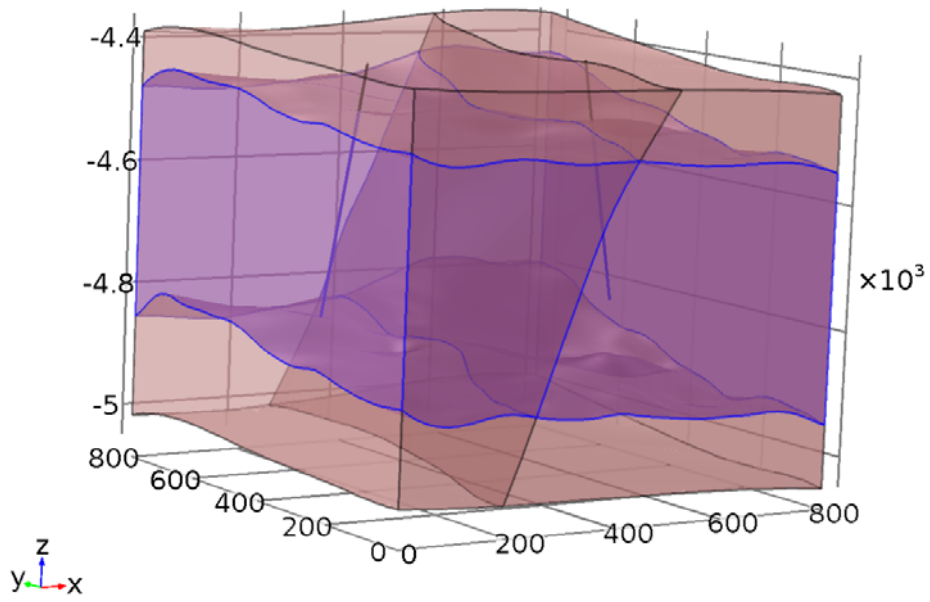
915
916
917
918
919



920
921
922
923

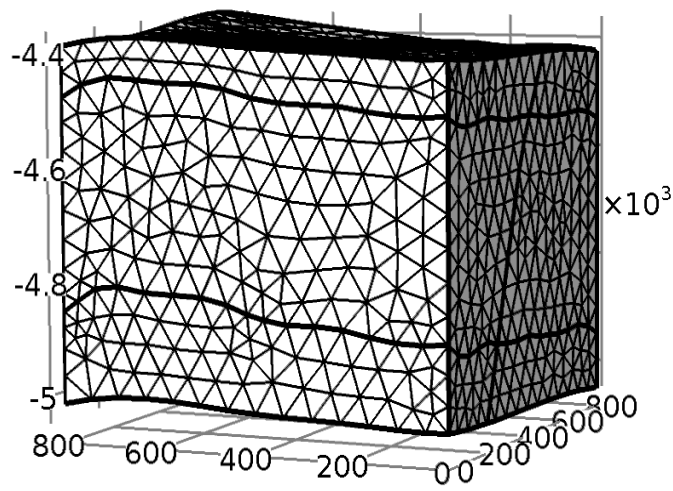
Figure 4: Pressure profile along a diagonal line from the bottom-left passing via the fracture to the top-right

924
925
926
927



928
929
930

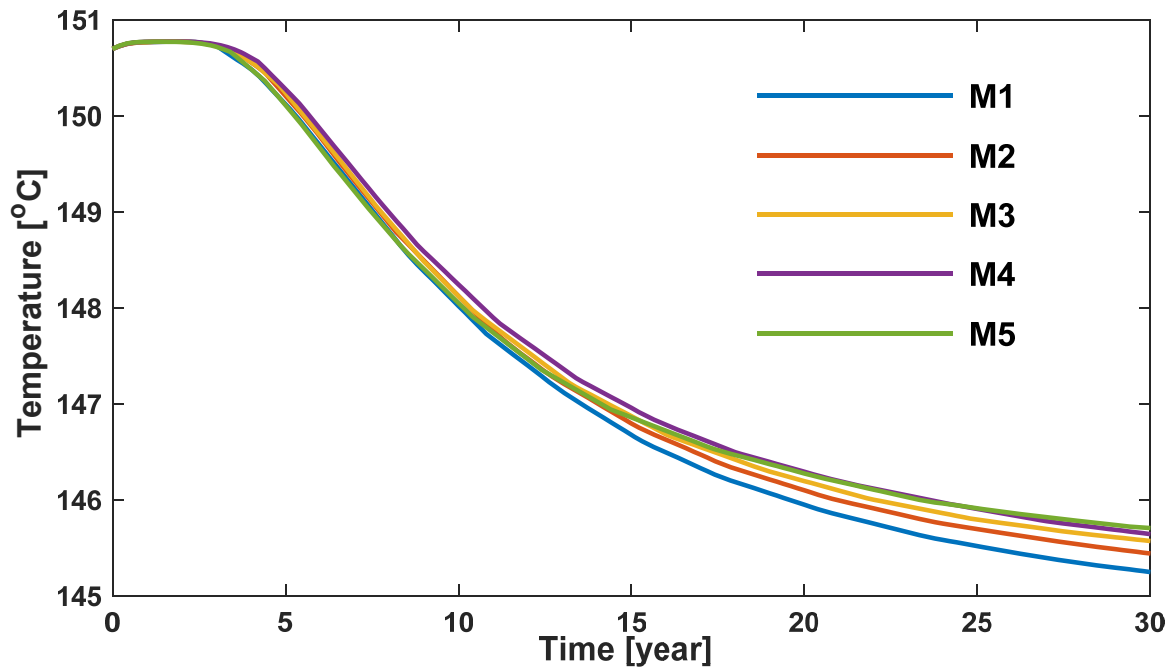
Figure 5(a): Reservoir geometry



931
932
933

Figure 5(b): Reservoir mesh

934

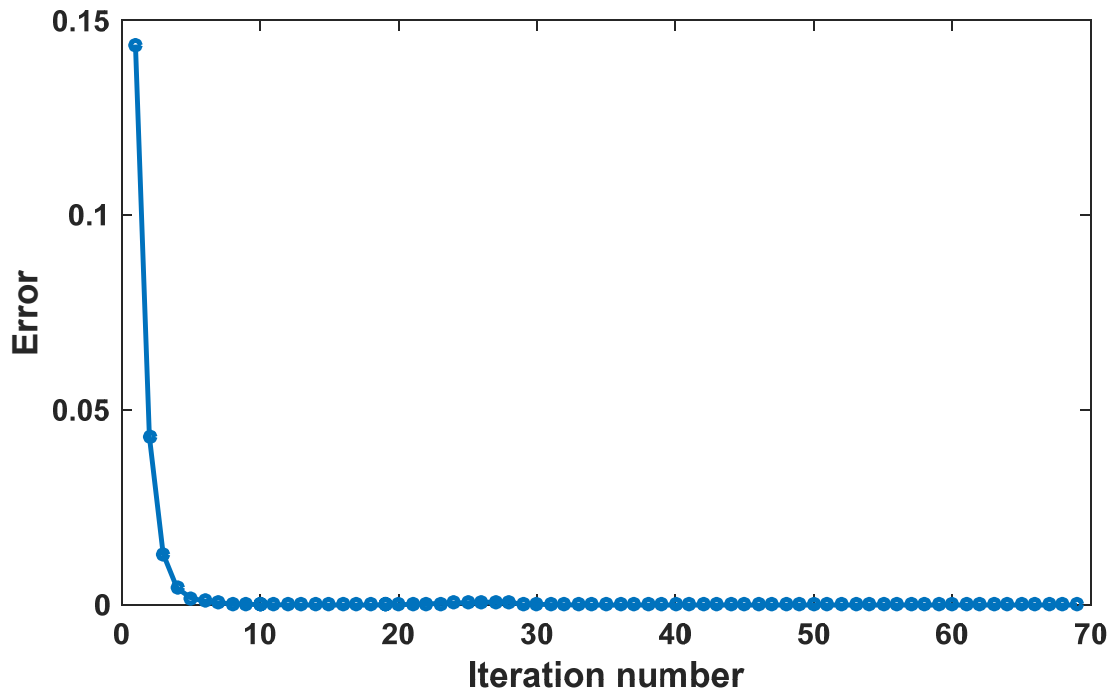


935

936

Figure 5(c): Mesh convergence study

937



938

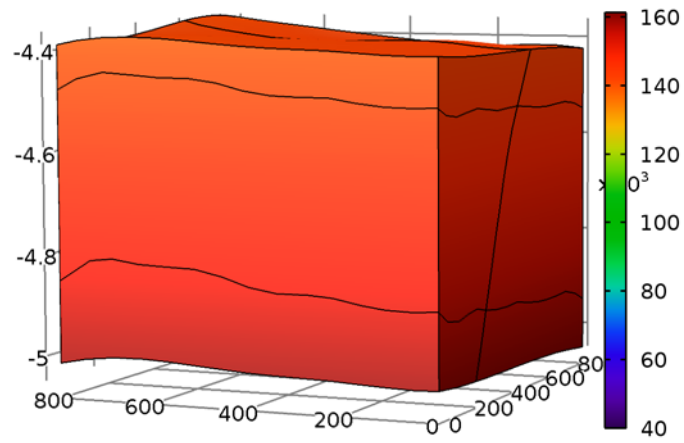
939

Figure 5(d): Error estimation

940

Figure 5: Case study of the geothermal reservoir model, mesh with the solution convergence

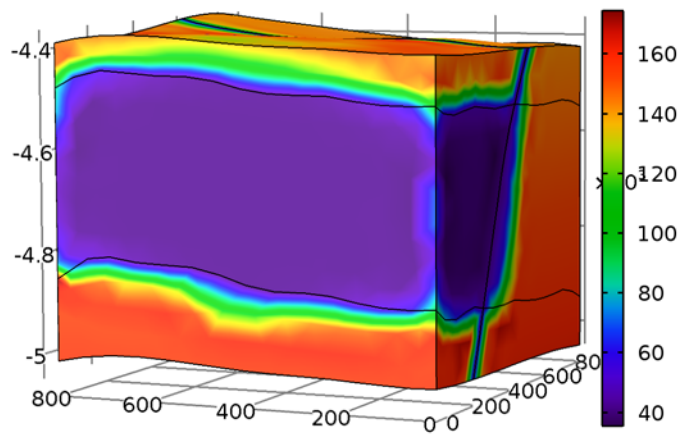
941



942

943

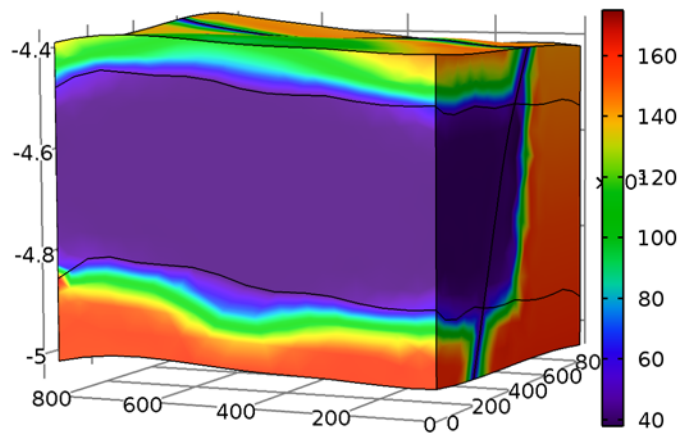
(a) At 0 year



944

945

(b) After 15 year



946

947

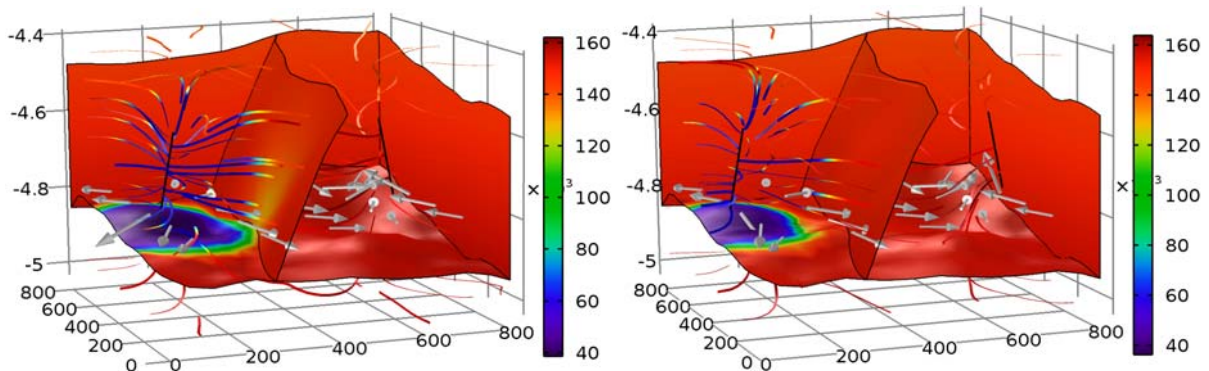
(c) After 30 year

948

Figure 6: Matrix cold water front distribution ($^{\circ}\text{C}$) at different stages of simulations

949

950

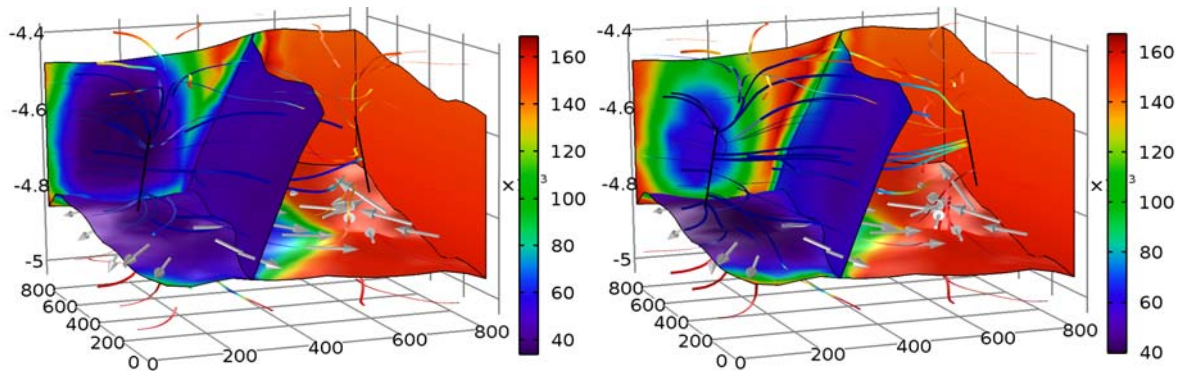


951

(a) 600 m well spacing at 1 year

(b) 700 m well spacing at 1 year

953



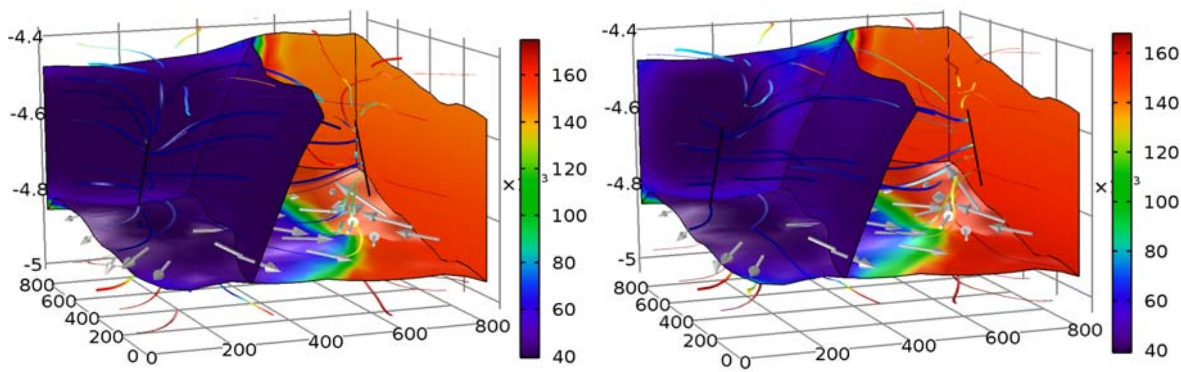
954

(c) 600 m well spacing at 15 years

(d) 700 m well spacing at 15 years

955

956



957

(e) 600 m well spacing at 30 years

(f) 700 m well spacing at 30 years

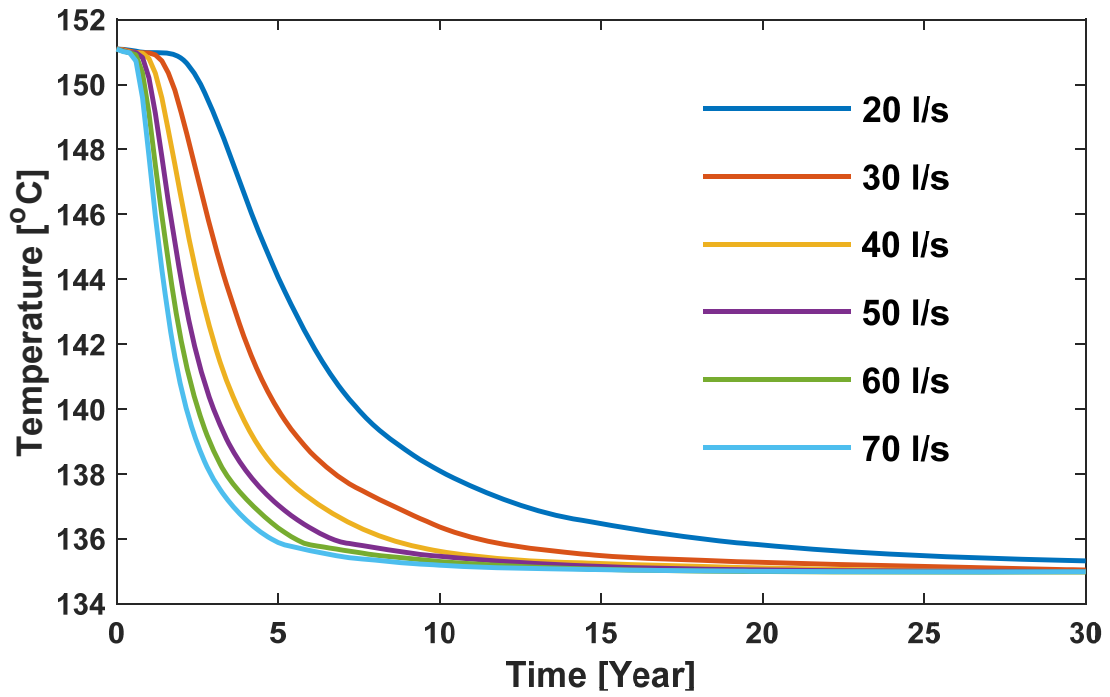
958

959 **Figure 7:** Cold water front propagation within the reservoir ($^{\circ}\text{C}$) for different well spacing at

960 various stages of simulations

961

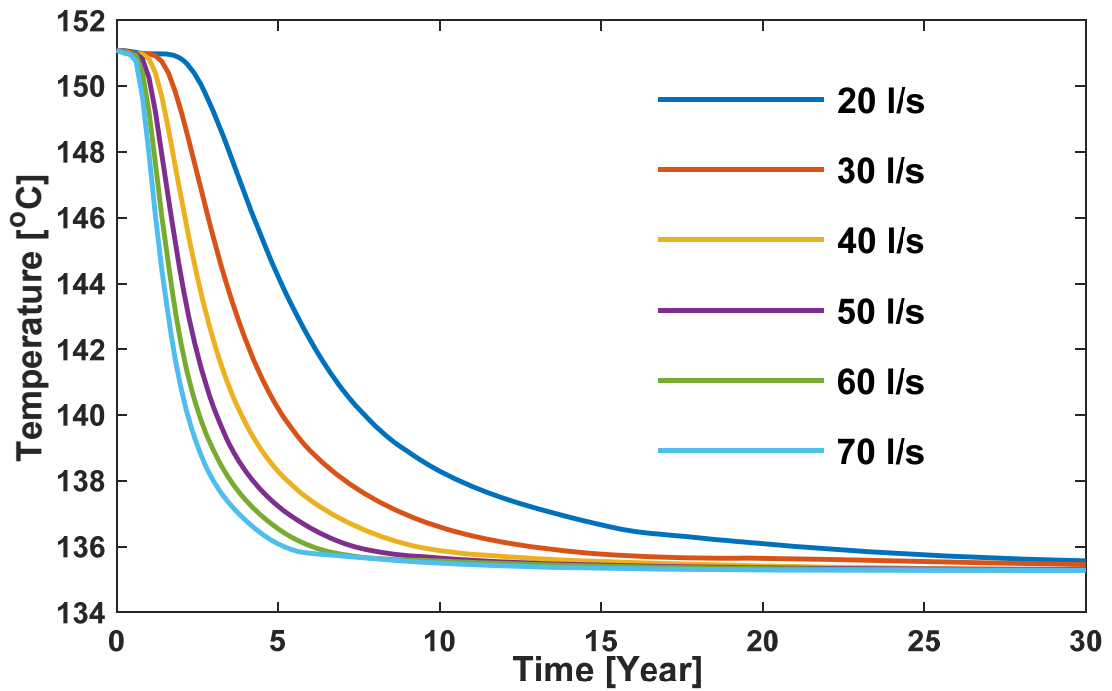
962



963

964

(a) Fluid injection temperature 40°C with 600 m lateral well spacing



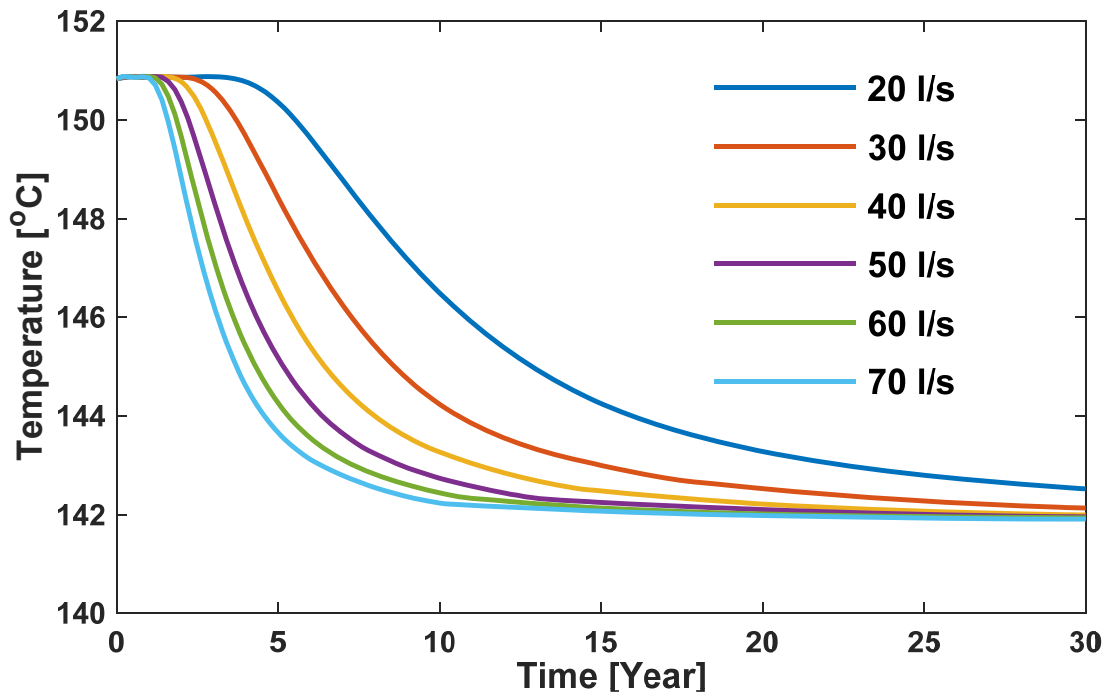
965

966

967

968

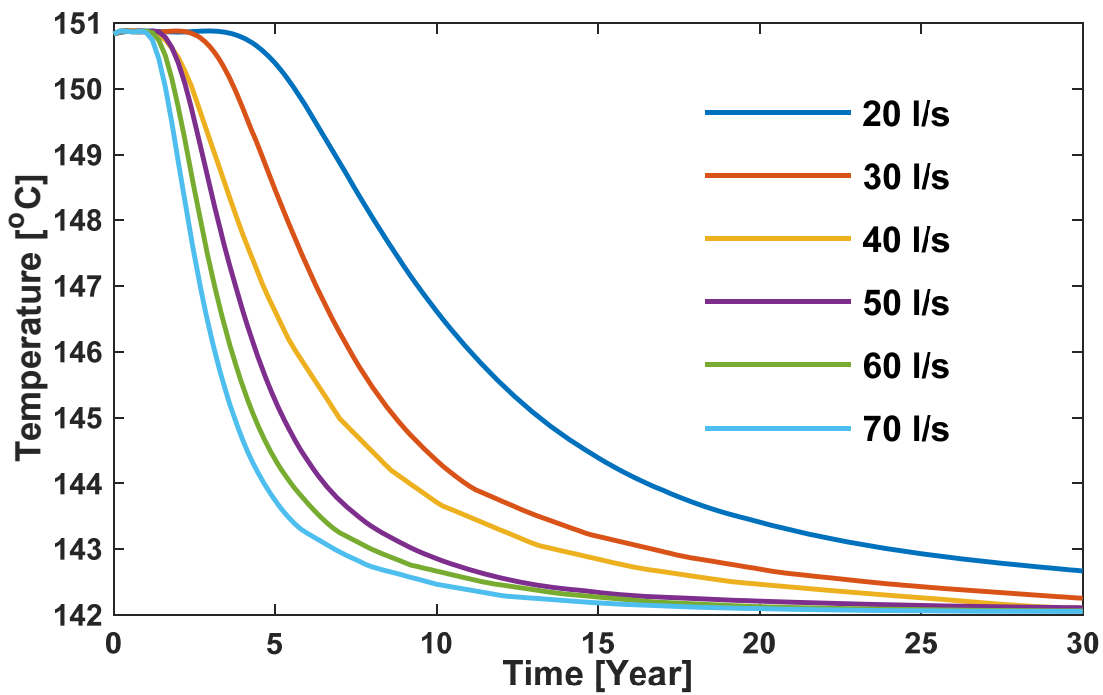
(b) Fluid injection temperature 50°C with 600 m lateral well spacing



969

970

(c) Fluid injection temperature 40°C with 700 m lateral well spacing



971

972

(d) Fluid injection temperature 50°C with 700 m lateral well spacing

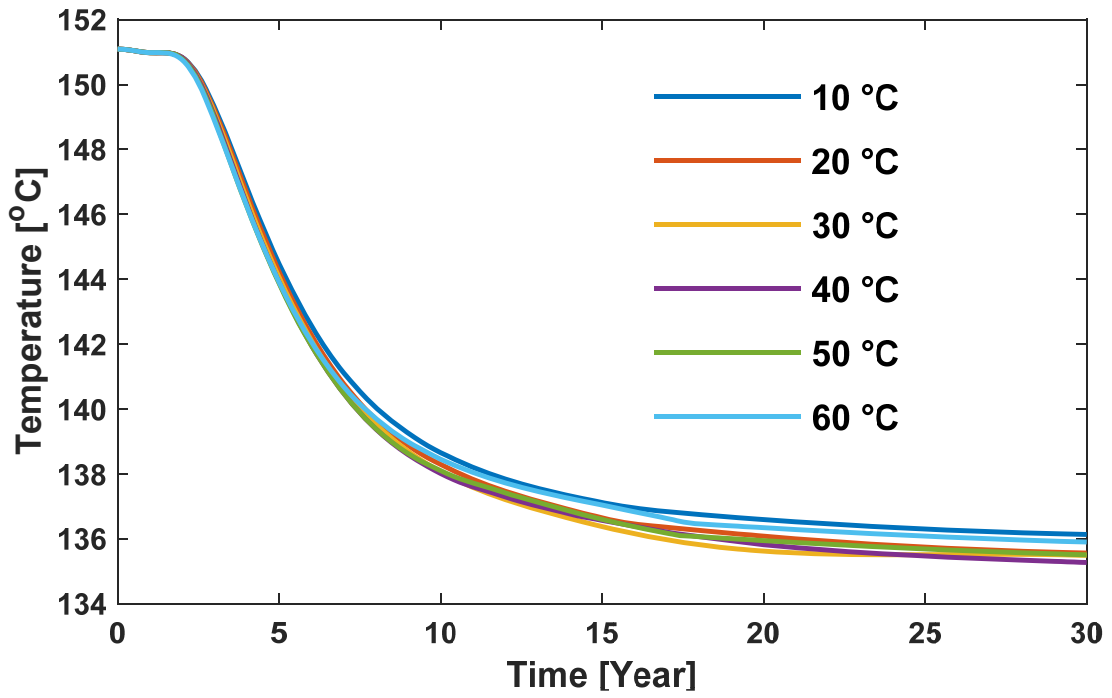
973

Figure 8: Production wellhead temperature under the effect of various injection flow rate ranging from 20 to 70 l/s

974

975

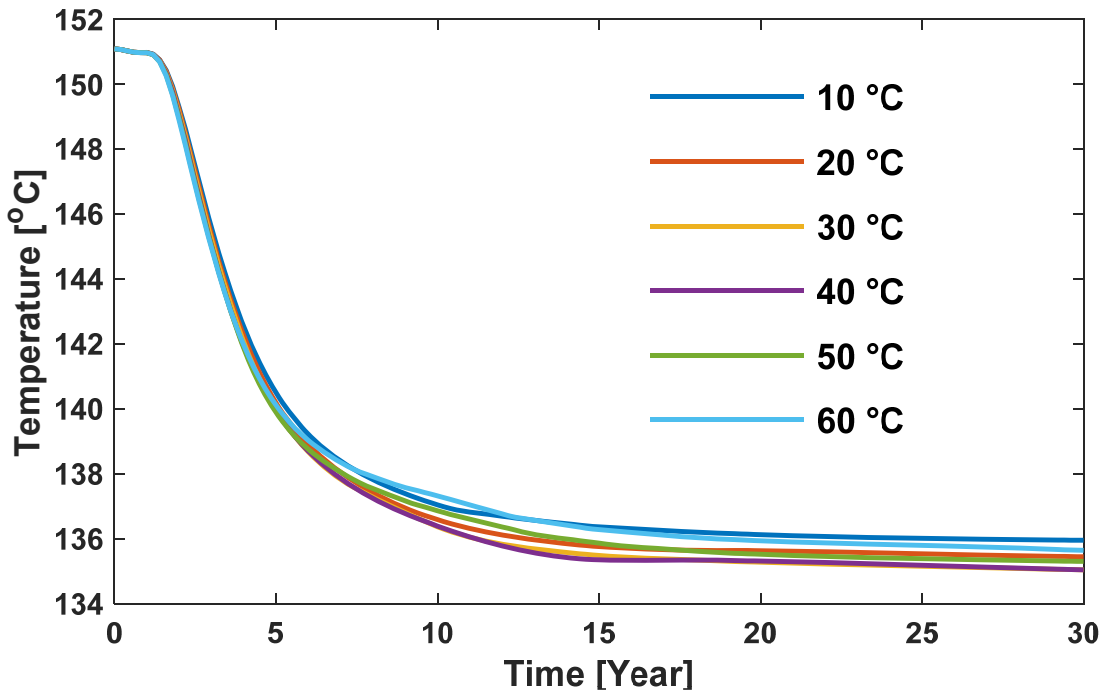
976



977

978

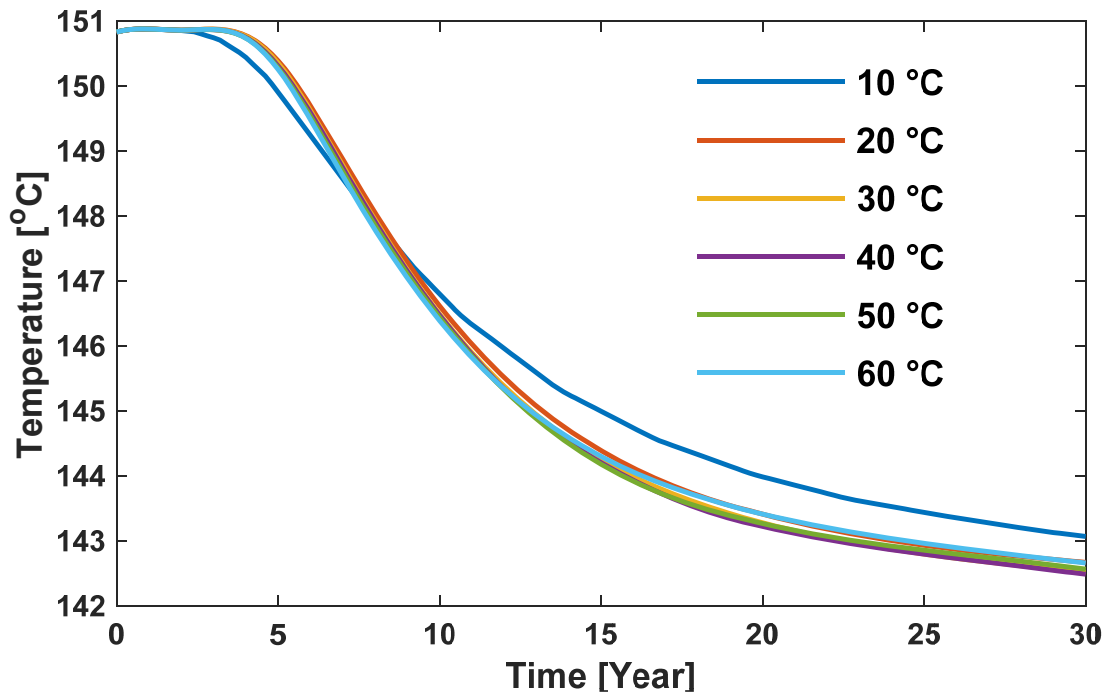
(a) Fluid injection rate 20 l/s with 600 m lateral well spacing



979

980

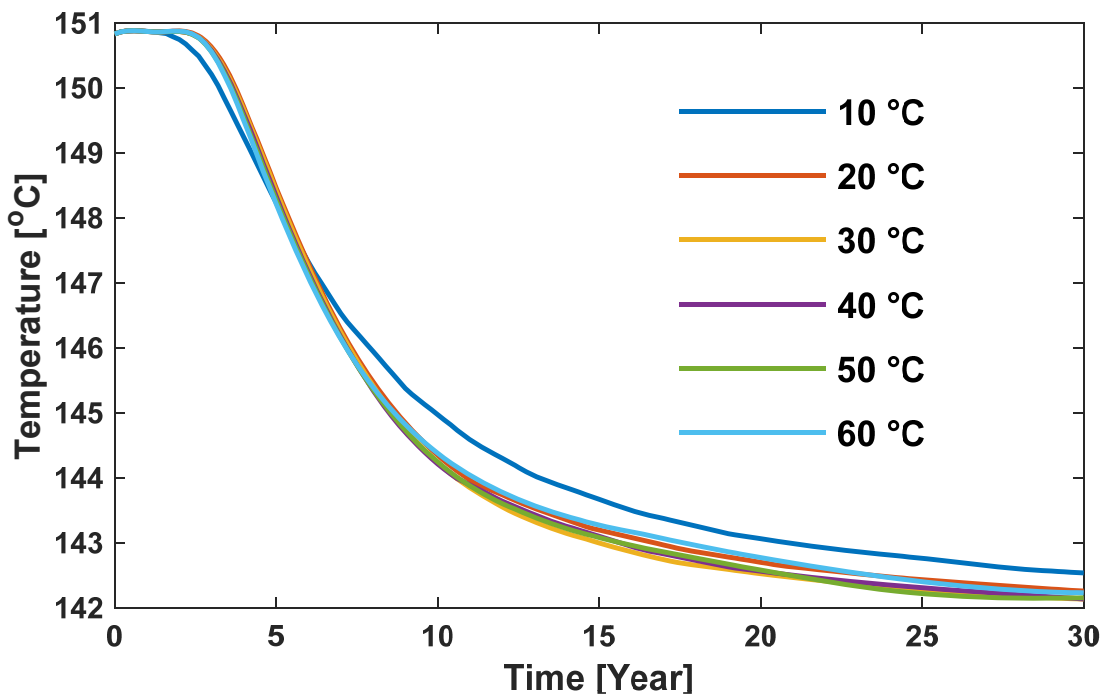
(b) Fluid injection rate 30 l/s with 600 m lateral well spacing



981

982

(c) Fluid injection rate 20 l/s with 700 m lateral well spacing



983

984

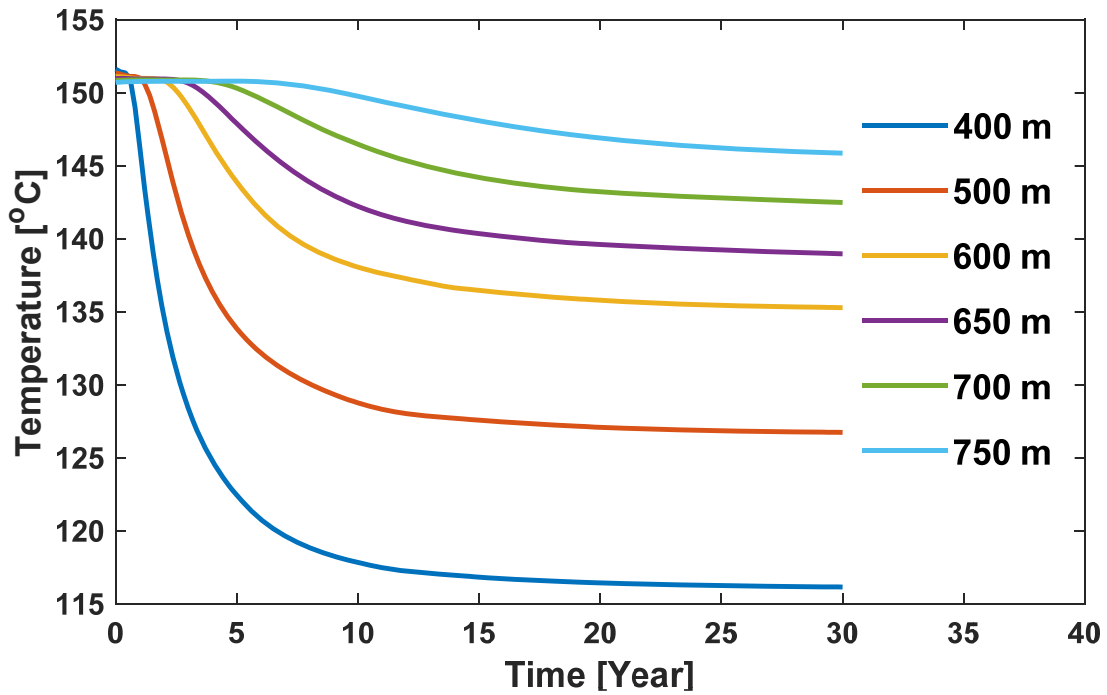
(d) Fluid injection rate 30 l/s with 700 m lateral well spacing

Figure 9: Production temperature over time due to the effect of various injection fluid temperatures ranging from 10°C to 60°C

986

987

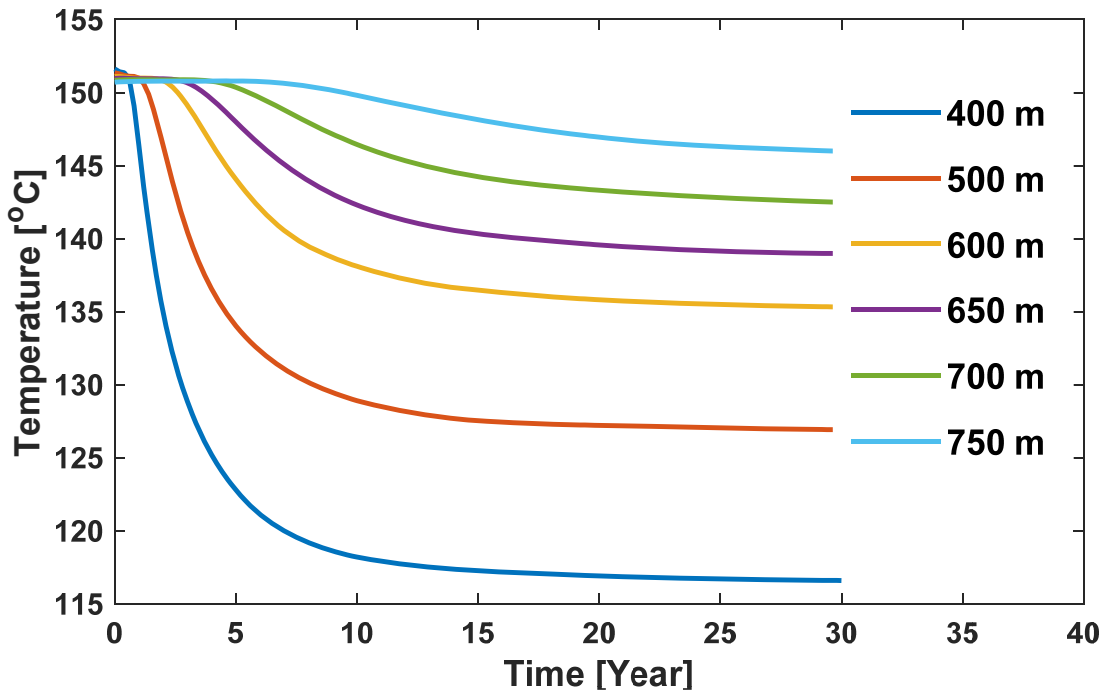
988



989

990

(a) Fluid injection rate 20 l/s with 30°C injection fluid temperature

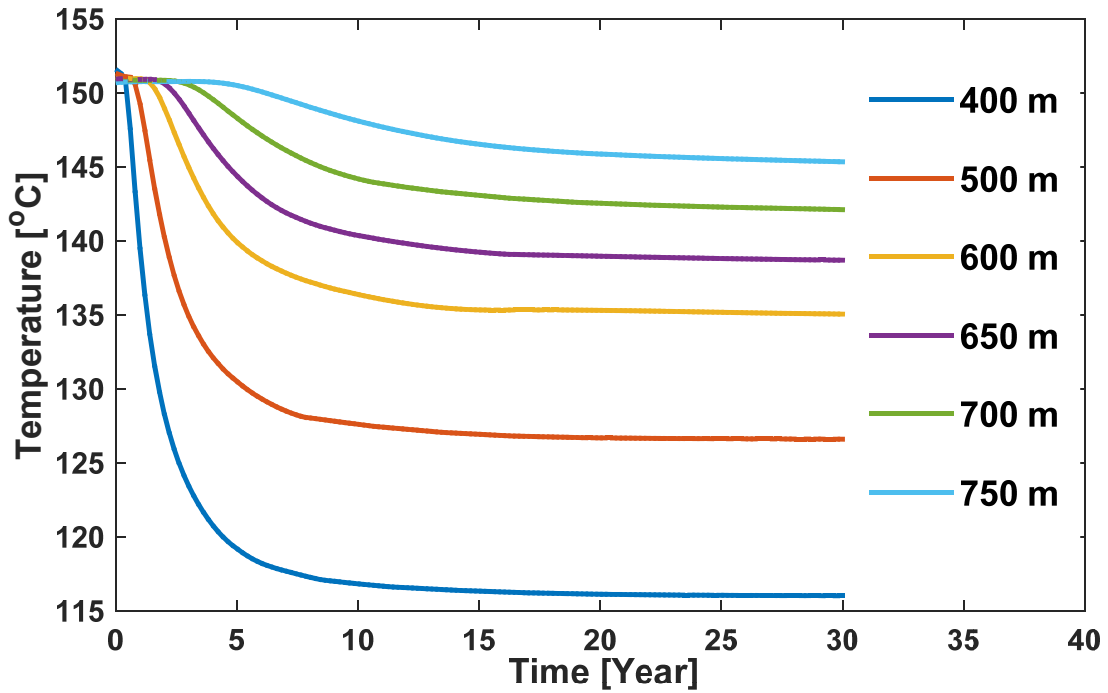


991

992

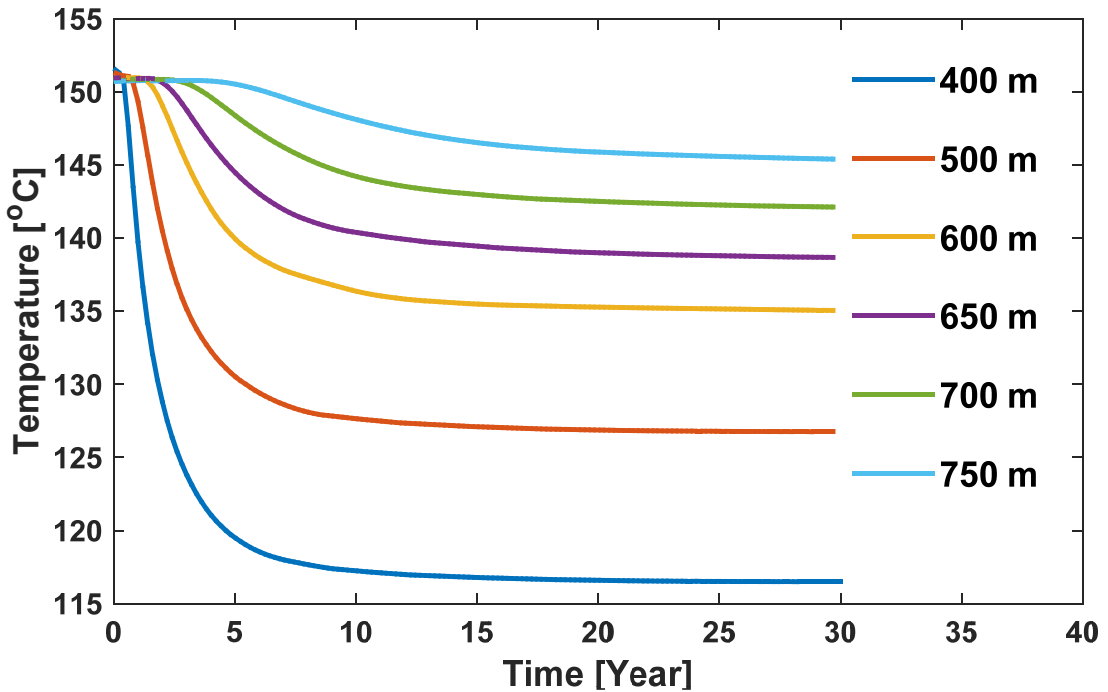
993

(b) Fluid injection rate 20 l/s with 40°C injection fluid temperature



994
995

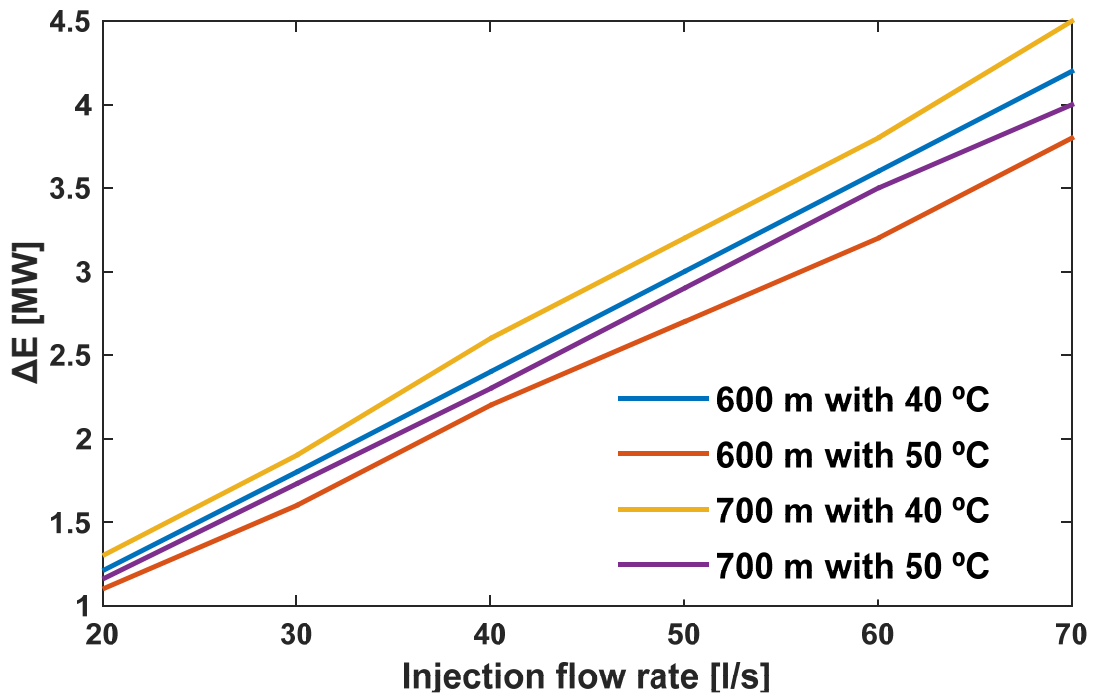
(c) Fluid injection rate 30 l/s with 30°C injection fluid temperature



996
997

(d) Fluid injection rate 30 l/s with 40°C injection fluid temperature

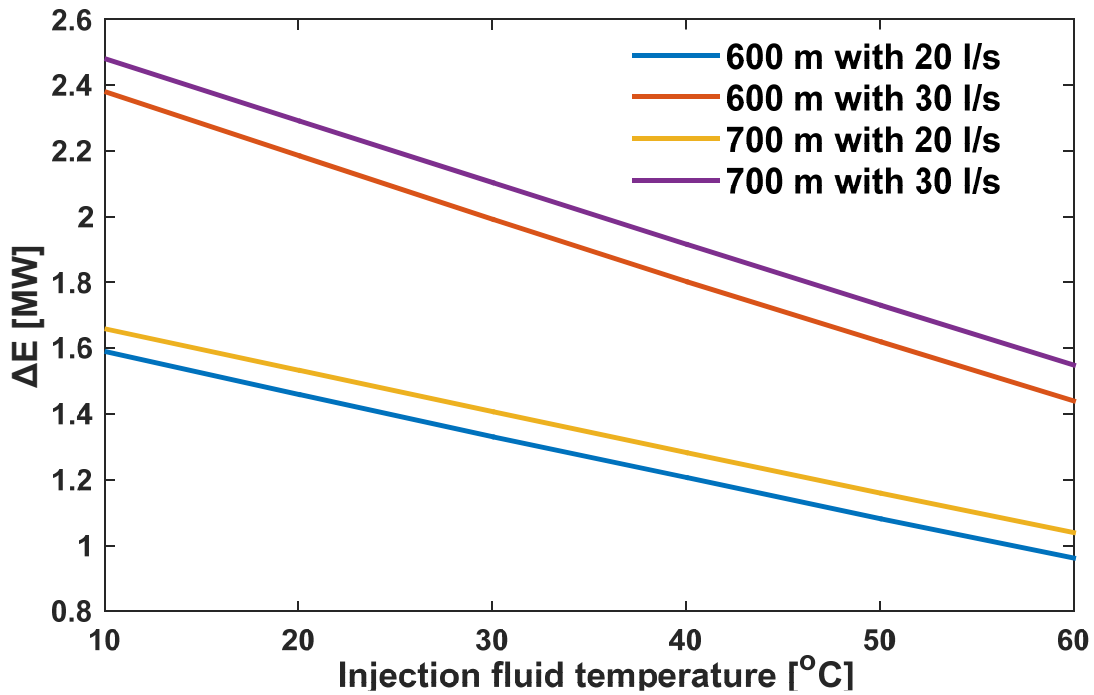
998 **Figure 10:** Production temperature over time due to the effect of various lateral well spacing



999

1000 **Figure 11:** Production energy as function of fluid injection rate under different lateral well
 1001 spacing and fluid injection temperatures

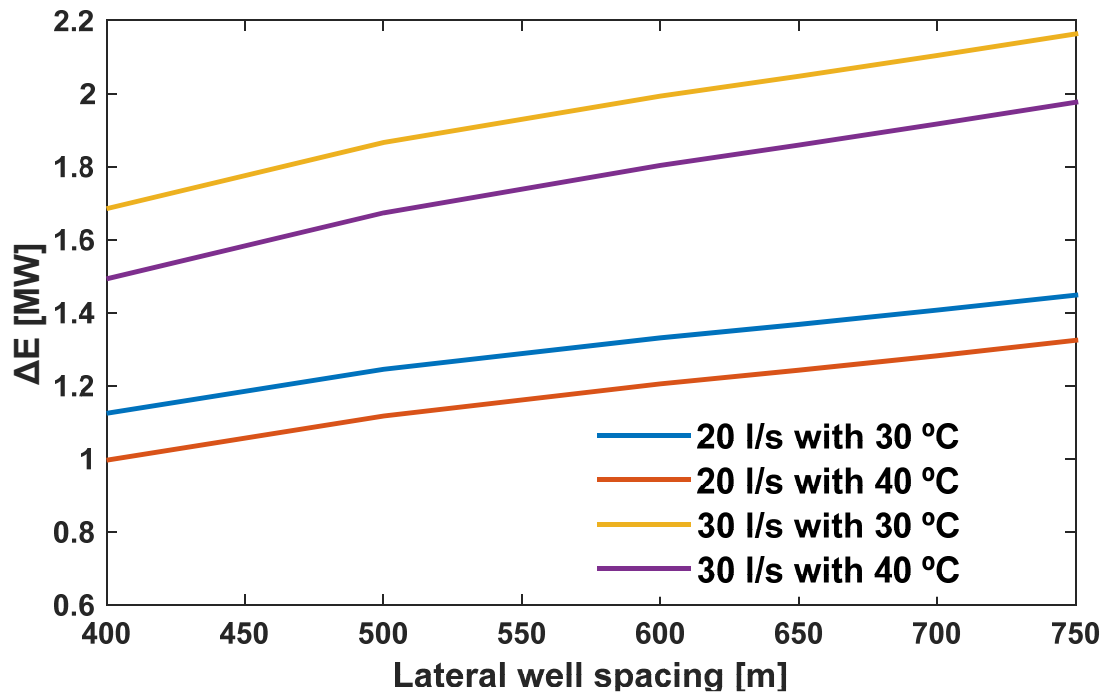
1002



1003

1004 **Figure 12:** Production energy as function of fluid injection temperature under different lateral
 1005 well spacing and fluid injection rates

1006
1007
1008
1009
1010
1011



1012
1013
1014
1015
1016
1017

Figure 13: Production energy as function of lateral well spacing under different injection flow rates and fluid injection temperatures